



Deposited via The University of Leeds.

White Rose Research Online URL for this paper:

<https://eprints.whiterose.ac.uk/id/eprint/185961/>

Version: Accepted Version

Article:

Wang, S, Nissen, E, Pousse-Beltran, L et al. (2022) Structural controls on Coseismic rupture revealed by the 2020 Mw 6.0 Jiashi earthquake (Kepingtag belt, SW Tien Shan, China). *Geophysical Journal International*. ggac159. ISSN: 0956-540X

<https://doi.org/10.1093/gji/ggac159>

© 2022, Oxford University Press. This is an author produced version of an article, published in *Geophysical Journal International*. Uploaded in accordance with the publisher's self-archiving policy.

Reuse

Items deposited in White Rose Research Online are protected by copyright, with all rights reserved unless indicated otherwise. They may be downloaded and/or printed for private study, or other acts as permitted by national copyright laws. The publisher or other rights holders may allow further reproduction and re-use of the full text version. This is indicated by the licence information on the White Rose Research Online record for the item.

Takedown

If you consider content in White Rose Research Online to be in breach of UK law, please notify us by emailing eprints@whiterose.ac.uk including the URL of the record and the reason for the withdrawal request.

1 **Structural controls on coseismic rupture revealed by the 2020**

2 M_w **6.0 Jiashi earthquake (Kepingtag belt, SW Tian Shan,**

3 **China)**

4 Siyu Wang^{1*}, Edwin Nissen¹, Léa Pousse-Beltran^{1,2}, Timothy J. Craig³, Ruohong Jiao¹,

and Eric A. Bergman⁴

¹*School of Earth and Ocean Sciences, University of Victoria, Victoria V8P 5C2, British Columbia, Canada*

²*Institute des Sciences de la Terre, Université Grenoble Alpes, 38058 Grenoble, France*

³*School of Earth and Environment, COMET, Institute of Geophysics and Tectonics, University of Leeds, Leeds, UK*

⁴*Global Seismological Services, Golden, CO 80401, USA*

5 8 April 2022

6 **SUMMARY**

7 The Kepingtag (Kalpin) fold-and-thrust belt of the southern Chinese Tian Shan is character-
8 ized by active shortening and intense seismic activity. Geological cross-sections and seismic
9 reflection profiles suggest thin-skinned, northward-dipping thrust sheets detached in an Upper
10 Cambrian décollement. The January 19 2020 M_w 6.0 Jiashi earthquake provides an oppor-
11 tunity to investigate how coseismic deformation is accommodated in this structural setting.
12 Coseismic surface deformation resolved with Sentinel-1 Interferometric Synthetic Aperture
13 Radar (InSAR) is centered on the back limb of the frontal Kepingtag anticline. Elastic dis-
14 location modelling suggests that the causative fault is located at ~ 7 km depth and dips $\sim 7^\circ$
15 northward, consistent with the inferred position of the décollement. Our calibrated relocation
16 of the mainshock hypocenter is consistent with eastward, unilateral rupture of this fault. The
17 narrow slip pattern (length ~ 37 km but width only ~ 9 km) implies that there is a strong struc-

18 tural or lithological control on the rupture extent, with up-dip slip propagation possibly halted
19 by an abrupt change in dip angle where the Kepingtag thrust is inferred to branch off the
20 décollement. A depth discrepancy between mainshock slip constrained by InSAR and teleseis-
21 mic waveform modelling (~ 7 km) and well-relocated aftershocks (~ 10 – 20 km) may suggest
22 that faults within sediments above the décollement exhibit velocity-strengthening friction.

23 **Key words:**

24 Radar interferometry, Asia, Earthquake source observations, Waveform inversion, Folds and
25 folding, Intra-plate processes

26 **1 INTRODUCTION**

27 Late Cenozoic crustal deformation in central Asia is dominated by reverse and strike-slip faulting
28 and folding within and around the margins of the Tian Shan mountains. Geodetic data indicate
29 that ~ 6 – 9 mm/yr of the present-day shortening occurs across the Chinese Tian Shan between the
30 northwestern Tarim Basin and southern Kyrgyzstan (Reigber et al., 2001; Wang et al., 2020). The
31 Kepingtag (Kalpin) fold-and-thrust belt has developed along part of the southern margin of this
32 range (Fig. 1). This actively-deforming belt is one of the most earthquake-prone regions of the
33 Tian Shan and of China. In recent years, this intense seismicity has attracted much interest in the
34 deformation style, rate and other characteristics of the Kepingtag belt (Allen et al., 1999; Zhou &
35 Xu, 2000; Zhang et al., 2008; Yang et al., 2002, 2006; Ran et al., 2006). Furthermore, it is one of
36 the few parts of Tian Shan where deformation can be seen stepping into the surrounding foreland,
37 with emergent thrust sheets predominantly vergent toward the Tarim basin in the south. Therefore,
38 the deformation of the Kepingtag belt can also inform how the mountain ranges of southern Tian
39 Shan grow through time.

40 Fold-and-thrust belts pose distinct challenges for seismic hazard assessment since much of
41 the active faulting is buried. This is exemplified by iconic earthquakes such as the 1978 M_s 7.4
42 Tabas, Iran earthquake (Walker et al., 2003) and the 1987 M_w 5.9 Whittier and 1994 M_w 6.7
43 Northridge, California earthquakes (e.g., Davis et al., 1989; Jones et al., 1994), each characterized

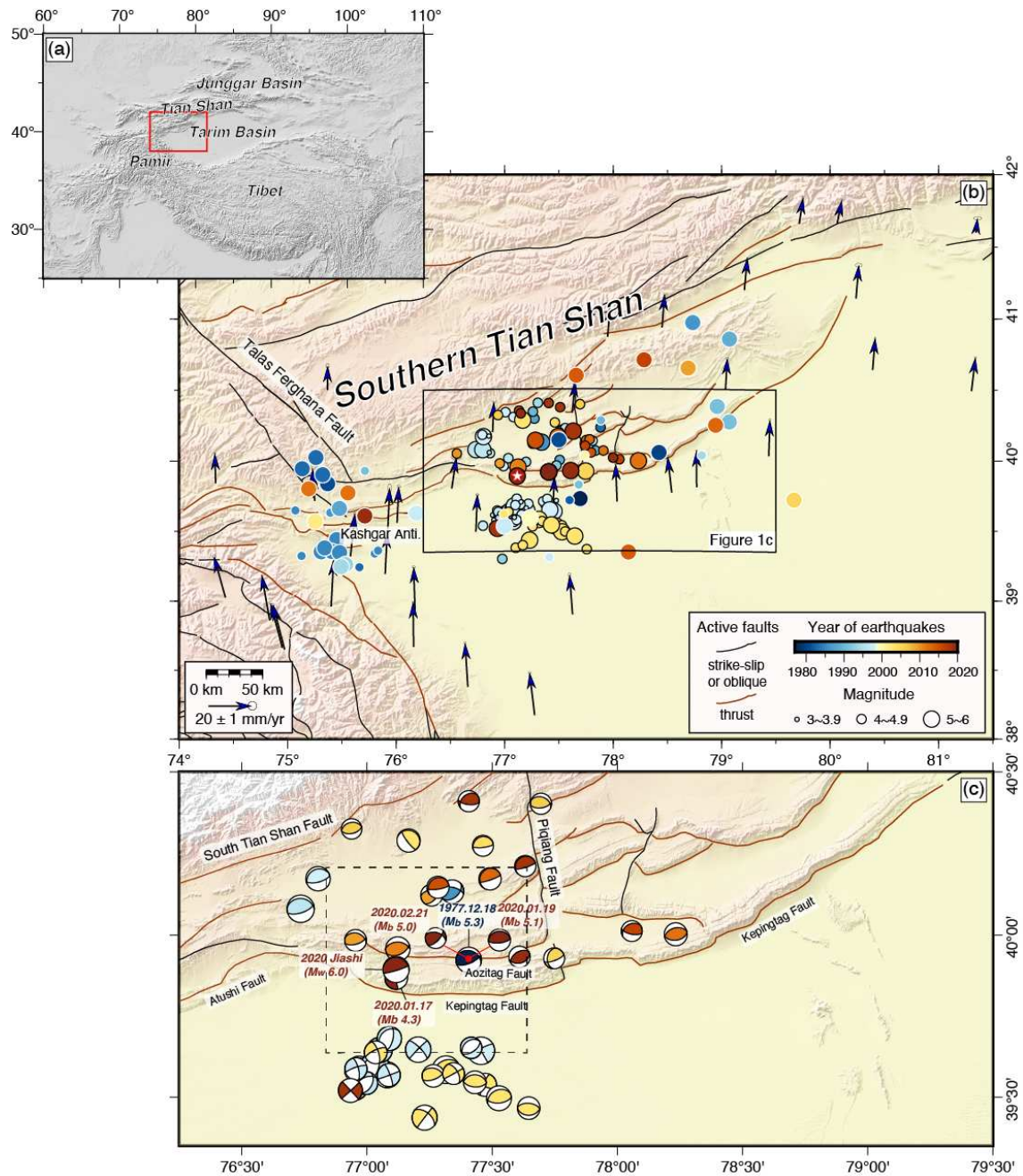


Figure 1. Tectonics and seismicity of the study area. (a) Shaded relief of the Himalayan orogeny with the location of panel (b) outlined in red. (b) Tectonic map of the southern Tian Shan. Instrumental seismicity is scaled by magnitude and colored by year from 1977.12.18 to 2020.02.21. Our own relocated epicenters are shown with black outlines, while those from the United States Geological Survey (USGS) have white outlines. The white star is the relocated epicenter of the 2020 January 19 Jiashi mainshock. Active faults are from the online database provided by the Institute of Geology, China Earthquake Administration (<http://www.neotectonics.cn/arcgis/apps/webappviewer/index.html?id=3c0d8234c1dc43ea0bec3ea03bb00bc>) and Global Navigation Satellite Systems (GNSS) velocities relative to stable Eurasia are from Wang et al. (2020) with 95% confidence ellipses. (c) Topography, active faults, and earthquakes of the Kepingtag fold-and-thrust belt. Focal mechanisms are from teleseismic body-waveform modelling studies or the Global Centroid Moment Tensor (CGMT) catalog (see Table 1 for details). They are plotted at our relocated epicenters, coloured by year and scaled by magnitude. The black dashed box shows the location of Figure 2.

44 by shallow folding and blind faulting without accompanying surface rupture. There are many
45 other examples of large earthquakes that ruptured faults that were not previously mapped, and
46 where historical and instrumental records were too short to have revealed the associated seismic
47 hazard beforehand. Furthermore, fold-and-thrust belts contain a wide range of fault structures
48 including décollements and ramp-and-flat thrusts, and it is often not clear which of these host large
49 earthquakes and which creep aseismically (e.g., Copley, 2014; Ainscoe et al., 2017; Mallick et al.,
50 2021). It is also important to consider how subsurface structure and stratigraphy may influence
51 rupture extents, and thus potential earthquake magnitudes (e.g., Elliott et al., 2011; Nissen et al.,
52 2011).

53 On January 19 2020 at 13:27:56 UTC, a M_w 6.0 earthquake struck near Jiashi in the west-
54 ern Kepingtag belt ($\sim 39.83^\circ\text{N}$, 77.21°E) (Fig. 1), causing intense ground shaking and damage
55 to hundreds of buildings. A regional seismic network recorded 1,639 aftershocks as of Febru-
56 ary 11 2020 (Ran et al., 2020), with the largest (M_b 5.1) occurring ~ 1 hour after the mainshock.
57 This sequence provides an opportunity to investigate patterns of seismicity and deformation in this
58 region. Routine teleseismic moment tensor solutions for the mainshock from the U.S. Geological
59 Survey (USGS) and the Global Centroid Moment Tensor project (GCMT) implicate thrust or re-
60 verse faulting, but exhibit discrepancies of tens of degrees in strike, dip, and rake and of several
61 kilometers in centroid depth and location. This makes it difficult to associate the earthquake with
62 specific faulting or characterize its tectonic implications without further investigation (Engdahl
63 et al., 2006; Weston et al., 2011; Wimpenny & Scott Watson, 2020).

64 Interferometric Synthetic Aperture Radar (InSAR) observations and modelling can provide
65 more precise constraints on fault geometries and depth extents of large, shallow continental earth-
66 quakes (e.g., Elliott et al., 2016). Furthermore, growing compilations of seismic phase arrival
67 times can help relocate earthquake hypocenters more accurately which, in conjunction with In-
68 SAR slip models, can provide additional information on rupture directivity (e.g., Pousse-Beltran
69 et al., 2020). In this paper, we map the surface deformation of the 2020 Jiashi earthquake using the
70 Sentinel-1 InSAR imagery and characterize its subsurface fault geometry and slip distribution us-
71 ing elastic dislocation modelling. We provide an independent check on its mechanism and centroid

72 depth using teleseismic body waveform modelling and pinpoint its hypocenter using a calibrated,
73 multi-event relocation. We relate some striking features of the surface deformation and slip model
74 to the subsurface structure of the Kepingtag belt. Our multi-event relocation also allows us to re-
75 assess earlier instrumental earthquakes in this region. These new results are used to reevaluate the
76 active tectonics and seismic hazard of the Kepingtag belt.

77 **2 TECTONIC SETTING**

78 The Tian Shan in Central Asia originally formed in the Paleozoic, and most of the present topog-
79 raphy of the mountain ranges resulted from Cenozoic reactivation as a result of the India-Eurasia
80 collision (Windley et al., 1990; Hendrix et al., 1992; Avouac & Tapponnier, 1993; Burchfiel et al.,
81 1999). Over time, the deformation has propagated outward into the Tarim and Junggar basins,
82 where along certain parts of the Tian Shan margins, intense folding and faulting have created sets
83 of narrow ridges. The Kepingtag fold-and-thrust belt, located along the arid southern margin of
84 the Chinese Tian Shan, offers one of the clearest examples of this basinward migration of active
85 deformation (Fig. 1b).

86 **2.1 Geology of the Kepingtag belt**

87 About 200 km long by 50 km wide and trending WSW–ENE, the Kepingtag belt consists of
88 fault-related folds associated with a series of south-verging, imbricated thrust stacks (Allen et al.,
89 1999). Folded strata are composed of Cambrian–Ordovician Qiulitag group limestones, Middle
90 Ordovician Saergan group limestone and dolomite, Silurian Kepingtag group sandstone, Devonian
91 sandstone, Carboniferous Kangkelin group sandstone, lower Permian limestone, and Paleogene–
92 Neogene Wuqia group sandstone and conglomerate (Chen et al., 2006; Yang et al., 2010). The
93 thickness of the upper Paleozoic strata in the Kepingtag belt increases from about 2 km in the
94 south to greater than 4 km in the north (Yin et al., 1998). There is a major angular unconformity
95 between the Paleozoic strata and the Cenozoic foreland basin deposits, with the near absence of
96 Mesozoic sedimentary rocks implying significant Paleozoic crustal shortening.

97 The thick Paleozoic sequence of mainly Upper Cambrian to Permian strata is exposed in

Table 1. Earthquake source parameters in the Kepingtag belt and its foreland. Relocated hypocenters are from this study. The focal depth (FD) is followed by a superscript letter describing how it was calibrated: *d* = teleseismic depth phases, *l* = local-distance readings, *n* = near-source station readings, and *c* = cluster default depths. Focal mechanisms are taken from (1) Fan et al. (1994), (2) Sloan et al. (2011), (3) Ghose et al. (1998), (4) the Global Centroid Moment Tensor (GCMT) catalogue, and (5) this study. The centroid depth (CD) is also given a superscript letter that describes whether it was obtained by modelling (*t*) teleseismic body-waveforms, (*d*) teleseismic depth phases, (*r*) regional waveforms, or (*i*) = InSAR surface displacements. Where only a less reliable GCMT centroid depth is available, we mark the solution with an asterisk.

Date	Time	Relocated hypocenter			Focal mechanism				M_w	Ref.
		Long.	Lat.	FD (km)	CD (km)	Strike	Dip	Rake		
1977.12.18	16:47	77.4065	39.9236	22 ^d	7 ^t	74	51	79	5.8	1
1986.04.25	16:12	77.3404	40.1340	13 ^d	15*	283	60	125	5.4	4
1996.03.19	15:00	76.7353	40.0810	13 ^l	34 ^t	234	16	87	6.0	2
1996.03.20	00:14	76.8644	40.0562	17 ^l	6 ^r	268	20	76	4.5	3
1996.03.22	08:26	76.7983	40.0816	15 ^l	6 ^r	260	18	78	5.2	3
1996.04.02	02:28	77.5587	40.2328	10 ^l	16 ^r	242	59	128	4.1	3
1997.01.21	01:48	77.2050	39.6475	11 ^l	12 ^t	317	85	177	5.4	2
1997.01.29	08:20	76.9678	39.5923	12 ^l	33*	04	83	132	5.2	4
1997.03.01	06:04	76.9532	39.5288	14 ^l	14 ^d	180	80	-173	5.6	2,4
1997.04.05	23:36	76.9622	39.5832	12 ^l	18 ^t	177	64	-139	5.4	2
1997.04.06	04:36	77.0809	39.5694	12 ^l	17 ^t	246	41	-74	5.8	2
1997.04.06	12:58	77.0324	39.6105	17 ^l	13 ^t	210	38	-74	5.1	2
1997.04.11	05:34	77.0326	39.6023	15 ⁿ	20 ^t	226	42	-79	6.0	2
1997.04.12	21:09	77.0039	39.5334	14 ⁿ	16 ^t	239	27	-74	5.1	2
1997.04.15	18:19	77.0506	39.6461	14 ⁿ	18 ^t	177	64	-139	5.7	2
1997.06.24	09:24	76.9562	39.5877	16 ⁿ	34*	345	72	-167	5.1	4
1997.10.17	17:35	77.0875	39.5686	25 ^d	33*	177	64	-139	5.3	4
1998.03.19	13:51	76.8048	40.1732	15 ^l	15 ^d	243	5	79	5.6	2,4
1998.08.02	04:40	77.0897	39.6817	10 ^d	15 ^t	173	40	-140	5.5	2
1998.08.03	15:15	77.0905	39.6527	15 ^l	29 ^r	253	10	129	4.6	2
1998.08.27	09:03	77.4554	39.6437	16 ^l	15 ^t	57	80	1	6.3	2
1998.09.03	06:43	77.4162	39.6528	25 ^d	10 ^r	179	59	178	4.8	2
1998.10.31	16:09	77.2469	39.6081	19 ^l	14 ^r	152	74	-164	4.6	2
2003.01.04	11:07	77.0350	39.6389	14 ^l	33*	245	73	-20	5.2	4
2003.02.24	02:03	77.3157	39.5852	19 ^l	5 ^t	280	17	115	6.2	2
2003.02.24	21:18	77.2653	39.5663	12 ^l	15*	289	33	126	5.2	4
2003.02.25	03:52	77.4717	39.5385	8 ^l	15*	239	33	62	5.3	4
2003.03.12	04:47	77.5273	39.4969	8 ^l	7 ^d	245	33	73	5.7	2,4
2003.03.15	22:59	77.3459	39.5733	9 ^l	15*	330	57	178	5.0	4
2003.03.30	23:15	77.4315	39.5462	17 ^l	10 ^t	287	27	117	5.2	2
2003.05.04	15:44	77.2305	39.4369	9 ^l	15*	308	53	179	5.8	4
2003.06.04	16:28	77.6458	39.4665	10 ^l	10 ^d	274	54	92	5.2	2,4
2003.09.26	23:35	77.1664	40.2902	30 ^d	15*	290	13	58	5.3	4
2004.10.07	16:14	77.4633	40.2740	12 ^l	17*	245	14	72	4.8	4
2005.03.24	07:37	77.7478	39.9288	11 ^d	30*	187	35	32	4.8	4
2006.06.08	11:34	77.6951	40.4025	6 ^d	30*	290	35	113	4.8	4
2006.09.06	07:51	76.9389	40.3257	15 ^l	32*	258	37	91	4.7	4
2009.04.22	09:26	77.2583	40.1229	11 ^d	16*	264	50	124	5.0	4
2009.10.16	02:56	76.9545	39.9836	15 ^d	19*	284	32	116	5.0	4
2011.08.11	10:06	77.1232	39.9575	19 ^d	12*	272	42	109	5.6	4
2012.08.11	09:34	78.2335	40.0027	15 ^d	12*	255	43	84	5.3	4
2013.03.11	03:01	77.4916	40.1729	9 ^d	12*	210	11	50	5.2	4
2015.01.10	06:50	77.2838	40.1469	14 ^c	15*	227	17	57	5.1	4
2016.07.09	16:36	78.0578	40.0128	14 ^c	12*	240	32	53	4.8	4
2018.04.12	10:41	77.4068	40.4104	17 ^l	22*	231	36	50	4.9	4
2018.09.03	21:52	76.9341	39.5211	14 ^c	15*	317	89	178	5.5	4
2018.11.03	21:36	77.6323	40.2120	14 ^c	12*	225	12	63	4.9	4
2019.01.06	16:22	77.6093	39.9331	6 ^d	12*	238	50	79	4.9	4
2020.01.17	16:05	77.1167	39.8682	12 ^d	21*	261	86	-178	5.3	4
2020.01.19	13:27	77.1161	39.8944	11 ^d	7 ⁱ	279	7	115	6.0	5
2020.01.19	14:23	77.4089	39.9236	14 ^c	18*	268	22	95	5.1	4
2020.02.21	15:39	77.4059	39.9232	14 ^c	14*	287	46	143	4.8	4

98 a series of parallel anticlines (Xinjiang Bureau of Geology and Mineral Resources, 1993). The
99 hanging wall cut-offs of the imbricate thrusts have been eroded away. This thrust system is inter-
100 preted as thin-skinned, with fault-propagation folds detached in Upper Cambrian limestones along
101 a décollement at ~6–10 km depth according to seismic reflection profiles and balanced geological
102 cross-sections (Allen et al., 1999; Yin et al., 1998; Nishidai & Berry, 1990; Yang et al., 2010).
103 The left-lateral Piqiang fault (Fig. 1) has developed perpendicular to the Kepingtag belt, dividing
104 it into two (western and eastern) segments. Interpretations of satellite imagery and balanced cross-
105 sections suggest that the thin-skinned imbricate thrusting and folding has accommodated crustal
106 shortening strains of 20–28% between the main Tian Shan and Tarim block, equivalent to ~35 km
107 across the western segment and ~22 km across the eastern segment (Allen et al., 1999; Yin et al.,
108 1998).

109 **2.2 Seismicity of the Kepingtag belt and its foreland**

110 Active crustal shortening and thickening of the southern Tian Shan is manifest in frequent reverse
111 faulting earthquakes that cluster around the margins of the high topography with nodal planes ori-
112 ented approximately parallel to the range (Ghose et al., 1998; Xu et al., 2006; Sloan et al., 2011).
113 The Kepingtag belt and its adjacent foreland are amongst the most seismically-active parts of the
114 Tian Shan, with thirty-six earthquakes of M_w 5.0–6.3 since the late 1970s (Fig. 1b and Table 1).
115 The 1902 M_w 7.7 Atushi (Kashgar) earthquake, located ~150 km west of our study area, hints
116 that much larger earthquakes may be possible (Kulikova & Krüger, 2017). Within the Keping-
117 tag belt, instrumental seismicity is concentrated west of the Piqiang fault and the available focal
118 mechanisms indicate a predominance of thrust and reverse faulting. Assuming that northward-
119 dipping nodal planes represent faulting, dip angles range from ~5°–60° with an average of around
120 30°. Only a few of these events have reliable centroid depths from detailed waveform modelling,
121 mostly in the range 6–16 km, consistent with faulting within the lower sedimentary cover and the
122 underlying basement (Fan et al., 1994; Ghose et al., 1998; Sloan et al., 2011). Sloan et al. (2011)
123 placed a single outlier event at 34 km depth, within the middle-to-lower crust, but noted that its

124 relatively complex waveforms could potentially be explained by a compound (multi-event) source
125 mechanism at a much shallower depth.

126 Between 1997 and 1998, thirteen earthquakes of M_w 5.0–6.3 struck the foreland south of the
127 Kepingtag belt. These included the destructive January–October 1997 Jiashi earthquake swarm ,
128 which caused 21 fatalities (Zhang et al., 1999). This sequence involved a mix of strike-slip and
129 normal faulting with well-resolved centroid depths of ~ 12 – 20 km (Sloan et al., 2011), as well as
130 some smaller, deeper earthquakes located by a temporary regional network but without reliable
131 focal mechanisms (Xu et al., 2006). The mechanisms and depths are challenging to interpret but
132 may reflect flexural rebound of the Tarim basin under loading from the Tian Shan (Sloan et al.,
133 2011). On February 24 2003, the M_w 6.2 Bachu–Jiashi earthquake struck the same area, result-
134 ing in 261 reported fatalities. In contrast with the 1997 swarm, the 2003 earthquake involved
135 northward-dipping thrust faulting with a much shallower centroid depth of ~ 5 – 7 km, interpreted
136 to represent southward propagation of the Kepingtag belt into the Tarim basin (Sloan et al., 2011).
137 It also produced an abundant aftershock sequence that was apparently concentrated in the middle
138 crust between ~ 15 – 25 km (Huang et al., 2006). Following the 2003 Bachu–Jiashi sequence, the
139 Kepingtag belt and its foreland entered a relatively quiescent period of seismic activity, with no
140 earthquake of magnitude 6 or above until the January 19 2020 event.

141 The 2020 Jiashi sequence occurred within the frontal, western Kepingtag belt. The sequence
142 was recorded by thirteen permanent stations at ~ 30 – 170 km distance and by two local stations
143 ~ 20 km SW and NW of the mainshock epicenter, which were deployed by the Xinjiang Earth-
144 quake Administration 4 and 18 hours after the mainshock, respectively. These regional recordings
145 have been used as the basis of three previous seismological studies of the sequence, summarized
146 below (Ran et al., 2020; Yao et al., 2021a; He et al., 2021). The M_w 6.0 mainshock was preceded
147 by two days of foreshock activity involving \sim N–S-oriented left-lateral strike-slip faulting. The
148 mainshock itself ruptured an \sim E–W-oriented thrust or reverse fault, though there is disagreement
149 amongst available seismological and geodetic models on its geometry and depth, which will be
150 discussed further in light of our own results in Section 4. The mainshock was followed by an
151 energetic aftershock sequence of several hundred events that lasted at least three months. Double-

152 difference relocated seismicity forms a ‘T’ shaped pattern in map view, with the mainshock located
153 at the bottom of the ‘T’ and aftershocks extending ~ 20 km northward to the junction of the ‘T’,
154 and from there, ~ 20 km east and west for a total length of ~ 40 km, with the greatest concentra-
155 tion of events along the western branch (Ran et al., 2020; Yao et al., 2021a; He et al., 2021). The
156 double differencing also shows that the aftershocks are concentrated at depths of 10–20 km (Figs.
157 S12 and S13).

158 **3 METHODS**

159 **3.1 InSAR measurements and modelling**

160 We used InSAR to measure surface deformation in the January 19 2020 earthquake, and elastic
161 dislocation modelling to estimate the fault geometry and slip distribution. The raw data are from
162 the European Space Agency’s C-band Sentinel-1A satellite, with wavelength ~ 5.6 cm. Two as-
163 cending tracks (056A and 129A) and one descending track (034D) capture the Jiashi mainshock.
164 Three, 12 day coseismic interferograms (January 11–23, January 16–28 and January 10–22 2020)
165 were processed using GAMMA software (Werner et al., 2000) and multi-looked to four looks in
166 range and twenty in azimuth to achieve a ~ 30 m \times 30 m pixel resolution. The topographic phase
167 contribution was removed using the 30 m-resolution Shuttle Radar Topographic Mission Digital
168 Elevation Model, which was also used to geocode the interferograms. The two ascending-track
169 interferograms were unwrapped using the branch-cut algorithm (Goldstein et al., 1988) while the
170 noisier, descending-track interferogram was unwrapped using the Minimum Cost Flow algorithm.

171 The interferograms exhibit excellent coherence, reflecting the dry desert conditions and sparse
172 vegetation of the southwestern Tian Shan. Coseismic surface deformation is easily distinguished
173 in all three interferograms as a double fringe ellipse elongated in an E-W orientation (Fig. 2a, d,
174 g). The southern lobe is focused on the Kepingtag anticline and exhibits up to ~ 7.5 cm of line-of-
175 sight (LOS) displacement toward the satellite, and the northern lobe is centered along the Aozitag
176 anticline and contains up to ~ 5 cm of displacement away from the satellite (Fig. 7a–c). The sim-
177 ilarity of the fringe patterns in ascending and descending interferograms implies that the largest
178 contribution to the observed LOS deformation is from uplift/subsidence rather than E/W lateral

189 displacement, consistent with predominantly dip-slip faulting. We also observe some localized
180 deformation along the southern Kepingtag rangefront its proximal foreland basin. The short wave-
181 lengths, and absence of shallow aftershocks in this area, hints that this deformation is caused by
182 secondary effects such as landsliding or liquefaction, and/or subsidence from agricultural activity
183 (e.g. through aquifer drawdown).

184 After downsampling the LOS displacements using a quadtree algorithm to concentrate sam-
185 pling in regions with high phase variance (Jónsson et al., 2002), we employed a routine, two-step
186 inversion strategy to estimate the causative fault parameters (e.g. Wright et al., 1999, 2004; Fun-
187 ning et al., 2005; Elliott et al., 2013, 2015; Ainscoe et al., 2017; Pousse-Beltran et al., 2020). In
188 the first step, we inverted the downsampled data to solve for the optimal strike, dip, rake, slip,
189 length, and top and bottom depths of a rectangular, uniform slip model fault plane buried within
190 an elastic half space; we also jointly solved for nuisance parameters (a static shift and linear ramp
191 in LOS displacement for each interferogram to account for their different unwrapping reference
192 points, satellite orbital errors, and long-wavelength lateral variations in tropospheric delay) and
193 weighted the single descending interferogram equal to the two ascending interferograms. We used
194 Okada’s expressions (Okada, 1985) to relate model fault slip to deformation of the free surface,
195 applied a non-linear, downhill Powell’s algorithm (Press et al., 1992) to obtain the minimum mis-
196 fit parameters, and ran 500 Monte Carlo restarts with random starting parameters to sample the
197 parameter space fully and avoid local minima (Wright et al., 1999). Without firm constraints on
198 how rheological properties vary with depth locally, we assumed an elastic half space with standard
199 Lamé parameters (λ and μ) of 3.2×10^{10} Pa. We anticipate that this assumption only moderately
200 impacts the retrieved fault parameters; for example, tests of layered and half-space elastic struc-
201 tures for a similar magnitude, buried earthquake in Tibet showed differences of $<1^\circ$ in fault strike
202 and dip, $\sim 6^\circ$ in rake, 0.2–0.5 km in fault length, top and bottom depths, and center coordinates,
203 and 5–8% in slip and moment (Bie et al., 2014). We also assumed a flat free surface, which is
204 appropriate given the limited (<1 km) relief across the study area and is not expected to impact
205 the retrieved fault parameters significantly (Li & Barnhart, 2020). Finding a trade-off between slip
206 and fault width — which is common for buried earthquakes (e.g. Funning et al., 2005; Elliott et al.,

207 2013) — we obtained the initial fault geometry by fixing slip to 1.0 m. Inversions performed with
 208 0.5 m, 1.5 m and 2.0 m show that this choice makes no significant difference to the resulting fault
 209 geometry, with variations of $<1^\circ$ in the resulting model fault strike, dip and rake, and <0.5 km in
 210 fault length and fault center point latitude, longitude and depth (Table S1).

211 In the second step, we estimated the slip distribution by extending the uniform slip model
 212 fault plane along strike and up- and down-dip, dividing it into $1 \text{ km} \times 1 \text{ km}$ sub-fault patches,
 213 and solving for slip on each patch (with rake fixed to the uniform slip solution) using a Laplacian
 214 operator to vary smoothing (Wright et al., 2004; Funning et al., 2005) and a non-negative least
 215 squares algorithm to ensure positive slip (Bro & De Jong, 1997). We solved for the best-fitting slip
 216 model and nuisance parameters, \mathbf{m} , using the equation,

$$217 \begin{pmatrix} \mathbf{G} \\ \kappa \nabla^2 \end{pmatrix} \mathbf{m} = \begin{pmatrix} \mathbf{d} \\ 0 \end{pmatrix}$$

218 where \mathbf{G} is the matrix of Green's functions (LOS displacements calculated at downsampled
 219 data locations using the formulation of Okada (1985) for 1 m of slip on each fault patch), ∇^2 is
 220 the finite difference approximation of the Laplacian operator which acts to smooth the distribution
 221 of slip, κ is a scalar smoothing factor which determines the relative importance of the smooth-
 222 ing operator, and \mathbf{d} contains the downsampled LOS displacements. We settled upon a preferred
 223 smoothing factor that represents a compromise between decreasing the fault slip roughness to
 224 prevent unrealistic, oscillating slip distributions, while minimizing the resulting increase in misfit
 225 (Wright et al., 2004). The resulting model still included a few outlier slip patches that lay sev-
 226 eral kilometers up-dip from the main slip distribution, which we consider spurious and exclude
 227 from our final, reported results. These are tabulated in Supplementary Table S3, and were used to
 228 generate the forward model and residual interferograms shown in Fig. 2.

229 Given the structural complexity of the Kepingtag belt, we also investigated whether the Jiashi
 230 earthquake may have involved non-planar rupture geometries by inverting the InSAR displace-
 231 ments for two uniform slip model fault planes (e.g., Pousse-Beltran et al., 2020). We explored a
 232 range of listric and anti-listric configurations by matching the top depth of a deeper model fault to
 233 the bottom depth of a shallower model fault, and allowing their dips to vary independently and up

234 to angles as steep as 32.5° . Though the large number of free parameters in these two-fault models
235 make it challenging to explore fully this parameter space, none of the two-fault configurations that
236 we tested produced a realistic geometry that improved upon the misfit of the simple, single-fault
237 model. This leads us to favour involvement of a single, planar fault.

238 We did not have access to GNSS data that could potentially constrain our slip model further,
239 though we know of six stations within ~ 100 km of the mainshock that may have exhibited coseis-
240 mic offsets (Figure 1; Wang et al. (2020)). Instead, we provide a table of displacements at these
241 sites predicted by our preferred, InSAR-derived distributed slip model (Supplementary Table S6).
242 These could be used for comparison by any future GNSS study of the Jiashi sequence.

243 **3.2 Calibrated hypocenter relocations**

244 We relocated hypocenters of the January 19 2020 Jiashi mainshock and its principal foreshock
245 (m_b 4.3) and two largest aftershocks (m_b 5.1 and 5.0) using teleseismic, regional and local seis-
246 mic phase arrival times. Thirty-seven well-recorded background events starting from 2003 were
247 also relocated, providing the repeated phase observations at common stations and the improved
248 azimuthal coverage at local distances needed to calibrate the cluster, by which we mean minimiz-
249 ing hypocentral biases from unknown Earth structure and reliably quantifying their uncertainties
250 (Bergman et al., submitted). We adopt the Hypocentroidal Decomposition relocation approach
251 of Jordan & Sverdrup (1981) which separates the relocation into two distinct inverse problems,
252 each reliant on customized phase arrival time data. We solve first for the relative locations of each
253 hypocenter with respect to the reference hypocentroid (defined as the arithmetic mean of all in-
254 dividual event hypocenters within the cluster) using arrival data at all distances, allowing us to
255 capitalize upon the abundance of teleseismic phase picks available for larger events in the cluster.
256 We then solve for the absolute location of the hypocentroid using only locally recorded, direct Pg
257 and Sg phases, which are impacted least by unknown Earth structure. This enables us to update the
258 absolute hypocenter coordinates of every event in the cluster. In other, comparably instrumented
259 regions, direct calibrations (ones that utilize local seismic data to solve for the hypocentroid) have
260 resolved epicenters to within ~ 1 – 2 km (at 90% confidence) and focal depths to within ~ 5 km

261 (Karasözen et al., 2019), improving substantially on the uncertainties of routine catalogs such
262 as the USGS and GCMT (Engdahl et al., 2006). Juxtaposing calibrated epicenters with InSAR-
263 derived slip models can distinguish bilateral from unilateral rupture propagation (e.g., Gaudreau
264 et al., 2019; Pousse-Beltran et al., 2020) and help resolve ambiguities in subsurface fault geome-
265 try, which are otherwise commonplace for buried earthquakes (e.g., Roustaei et al., 2010; Copley
266 et al., 2015; Elliott et al., 2015; Karasözen et al., 2018).

267 The cluster was relocated and calibrated in the *Mloc* program (Walker et al., 2011; Karasözen
268 et al., 2016; Bergman et al., submitted) using a customized travel-time model (Table S2) compris-
269 ing a 3-layered crust of thickness 50 km — consistent with several previous estimates of regional
270 Moho depths (Gao et al. (2013) and references therein) — over the upper mantle portion of the
271 global 1D model ak135 (Kennett et al., 1995). For the best-recorded events, we estimated focal
272 depths using local arrival times; for others, we relied upon teleseismic depth phases or simply
273 fixed the focal depth to a representative cluster default of 14 km (Fig. S1). We estimated the
274 hypocentroid using epicentral distances of up to 2° , for which there is excellent azimuthal cover-
275 age (Fig. S2); average residual travel times for phases used in this direct calibration are 0.0 sec
276 for *Pg* and 0.1 sec for *Sg* (Fig. S3). Observed phase arrivals and theoretical travel times for dis-
277 tances of up to 4° , 15° (for shear phases), and 30° are shown in Supplementary Figs. S4–S6. The
278 final relocated hypocenters, including epicentral uncertainties at 90% confidence, are provided in
279 Supplementary Table S3.

280 Our results were then combined with an earlier *Mloc* relocation cluster focused on the 1997
281 Jiashi earthquake swarm and the 2003 Bachu-Jiashi earthquake in the foreland south of the Keping-
282 tag belt (Bergman et al., submitted). The earlier cluster adopted the same relocation procedure and
283 the same regional velocity structure for the crust and upper mantle as this study. The earlier cluster
284 is available through the Global Catalog of Calibrated Earthquake Locations (GCCEL) database
285 (Bergman et al., submitted) and figures in the main paper incorporate both relocated datasets.

3.3 Teleseismic body waveform inversion

Finally, we used teleseismic body waveform modelling to provide additional constraints on the mainshock source depth and mechanism, complementing those from InSAR analysis. Modelling of both seismological and geodetic data is important when there are disagreements in the depth of faulting, as is the case for the Jiashi earthquake (see Section 4). Centroid depths obtained from waveform modelling can also help clarify whether fault slip resolved by InSAR models occurred coseismically or through afterslip (Nissen et al., 2014).

We followed the approach of Heimann et al. (2018), and inverted vertical and transverse component data from stations between 3,300 km and 9,900 km from the reported earthquake location (Supplementary Fig. S7). Waveforms were filtered between 0.01 and 1 Hz, and we used a window starting 15 seconds before, and ending 25 seconds after, the principle phase (*P* for vertical component waveforms, *S* for transverse component waveforms). Synthetic seismograms were generated using the velocity structure determined in our calibrated relocation (Section 3.2 and Supplementary Table S2). The source-time function is constrained to be a variable-duration half-sinusoid — appropriate for an earthquake of this size, and for the frequencies used in our inversions. Observed data and synthetics were aligned using cross correlation. The Bayesian approach outlined in Heimann et al. (2018) allows for the full sampling of the parameter space available in source depth, latitude, longitude, magnitude, and mechanism (Supplementary Figures S8–S9). Misfits between observed and synthetic waveforms are plotted in Supplementary Figures S10–S11.

4 RESULTS

Our best-fitting InSAR uniform slip model fault strikes 279° , dips 7° N, has a slight right-lateral component (rake 115°), and is ~ 22 km long by ~ 2 km wide, centered at 7 km depth (Table 2). To further test model sensitivity to centroid depth, we ran the inversion by prescribing different (fixed) top and bottom depths while allowing other parameters to vary freely. We also undertook similar tests of model sensitivity to dipping angle and fault width (aspect ratio). There is a fairly steep increase in misfit at fault center depths shallower or deeper than the minimum misfit value of 7 km (Fig. 3). For the equivalent dip sensitivity test, we find low misfits for dip angles of $5\text{--}10^\circ$,

313 but abrupt increases in root mean square error outside of this range (Fig. 4a). For the fault width
314 test, we find that extending the fault plane up- and down-dip leads to larger misfits, particularly
315 when the aspect ratio (length to width) is forced from the minimum misfit value of ~ 12 to below
316 ~ 6 . This shows that the highly-elongated model rupture area is real (Fig. 4b).

317 Compared to the uniform slip model, our preferred distributed slip model is longer at ~ 37 km
318 and wider at ~ 9 km, but remains centered at ~ 7 km depth (Fig. 5). The slip distribution is charac-
319 teristically narrow, with an aspect ratio (length to width) of around 4. The peak slip is ~ 0.5 m and
320 the model moment is $\sim 1.75 \times 10^{18}$ N. The resultant forward model interferogram matches the
321 observed surface deformation closely, with less than one residual fringe and a root mean square
322 residual of ~ 0.25 cm (Fig. 2c, f, i), which is substantially lower than that of the uniform slip model
323 (~ 0.35 cm). The close agreement between observed and forward model coseismic fringe patterns
324 implies that the more localized deformation along the Kepingtag range front had negligible impact
325 on our modelling.

326 Our InSAR model fault plane is 10° different in strike and 17° different in rake from the
327 N-dipping nodal plane of the USGS body-wave moment tensor, and there are even larger discrep-
328 ancies in strike and rake with the USGS W-Phase and GCMT solutions (Table 2). However, of
329 the four mechanisms the InSAR model strike is most closely aligned with \sim E–W trends in local
330 faulting, geological structure and topography. Furthermore, the shallow-dipping nodal planes of
331 the USGS and GCMT models are poorly constrained by teleseismic data and liable to be affected
332 by a strong trade-off between strike and rake (e.g. Beckers & Lay, 1995). Our distributed slip
333 model is 17–26% larger in moment than the three available seismological catalogue solutions.

334 Four other InSAR-derived fault models are also available for comparison (Table 2). Our model
335 is closest to that of He et al. (2021) and to the single fault solution of Yu et al. (2020); the three
336 models agree to within 4° in strike and dip, to within 6° in rake, and to within 1 km in centroid
337 depth. Yu et al.'s preferred, two-fault model is strongly listric, with slip apportioned between a
338 deep, gentle (2°) décollement and a much steeper (52°) ramp. However, we prefer the single-fault
339 solution, as the two-fault models we tested using different configurations of listric and antilistric
340 faults could not yield smaller misfits. Our model is ~ 2 km deeper and significantly shorter and

341 narrower than a uniform slip model by Yao et al. (2021b). However, they do not provide model or
342 residual interferograms, so there is no easy way to assess the accuracy of their model.

343 Our relocated mainshock hypocenter lies beneath the northern limb of Kepingtag anticline,
344 which is located ~ 6.6 km NNW from one inferred by Ran et al. (2020) using local data. How-
345 ever, our epicenter is somewhat closer to the InSAR-derived slip distribution patch, lying at its far
346 western end. Both our model and Ran et al. (2020)'s show that the Jiashi earthquake is strongly
347 unilateral, rupturing from west to east (Supplementary Fig. S12). Our relocated epicenter of the
348 January 17, 2020 m_b 4.3 foreshock lies ~ 3 km SE from the mainshock, and the two largest after-
349 shocks (m_b 5.1 and 5.0) lie near the eastern end of the mainshock model slip patch (Fig. 1c).

350 We show the results of our seismological inversions in Fig. 6 and synthetic waveforms for
351 all stations used in the inversion in Supplementary Fig. S10–S11. A probability density function
352 (PDF) of centroid depth results from an inversion with all parameters free shows both the mean and
353 the best-fit solution at just under 10 km (Fig. 6a). Using teleseismic data offers good constraints
354 on the mechanism only near the center of the focal sphere, where the pierce-points of teleseismic
355 body waves cluster. As such, the mechanism, and particularly the shallowly dipping nodal plane
356 are poorly constrained (inset mechanism, Fig. 6a). Consequently, we repeated the inversion using
357 double couple nodal planes fixed to match the InSAR-determined fault plane (Fig. 6b). This pushes
358 the PDF slightly deeper, with a mean depth at 11 km, but with a best-fit solution still at 10 km,
359 and makes only a marginal difference to the overall misfit values. We also show the PDF for the
360 seismologically-determined magnitude in Fig. 6c, which matches well with the inferred magnitude
361 of the geodetic signal. The model source time function duration of 8–10 seconds is rather long for a
362 M_w 6.0 thrust earthquake (e.g. Bayasgalan et al., 2005; Nissen et al., 2007; Elliott et al., 2015) and
363 supports our inference of unilateral rupture of a ~ 22 – 37 km fault assuming typical propagation
364 speeds of 1.5–4 km/s (Chounet et al., 2018).

365 In order to illustrate the constraints that the teleseismic data offer on the centroid depth, we
366 show a set of six example waveforms (three vertical components, three transverse component) and
367 best-fit synthetics calculated using three fixed centroid depths in Fig. 6d. The middle row shows
368 waveforms calculated at 10 km centroid depth, which is the best fit seismological solution, while

Table 2. Source parameters of the 2020 Jiashi mainshock inferred from our model and other sources. The longitude and latitude listed for our InSAR-derived models (first two rows) represent the surface projection of the model slip plane; our relocated epicenter is 77.117° E and 39.894° N. The other InSAR studies parameterize the fault location differently. Depths are given as the top, middle (or centroid) and bottom depths of the slip plane in that order. L and W are length and width, respectively. Yu et al. (2020) prefer their listric, two fault model with a deeper, flatter segment fixed at 2° dip and a shallower, steeper ramp at 52° . Yao et al. (2021b) used uniform slip of 0.32 m in their InSAR-derived model, which may account for their much larger model fault plane.

Source	Long.	Lat.	Strike	Dip	Rake	Depth (km)	L/W (km)	Moment (Nm)	M_w
This study, uniform slip	77.279°	39.902°	279°	7°	115°	7.0/7.1/7.2	22/2	1.31×10^{18}	6.0
This study, distributed slip	77.165°	39.416°	279°	7°	115°	6.3/7.0/7.6	37/9	1.75×10^{18}	6.0
USGS body-wave	77.11°	39.84°	262°	9°	105°	-/4/-	-	1.493×10^{18}	6.1
USGS W -phase	77.11°	39.84°	221°	20°	72°	-/19.5/-	-	1.387×10^{18}	6.0
CGMT	77.19°	39.80°	196°	38°	31°	-/11/-	-	1.39×10^{18}	6.0
Yu et al. (2020), 1 fault	77.30°	39.91°	275°	9°	111°	-/6.3/-	-	-	6.1
Yu et al. (2020), 2 faults	77.30°	39.90°	275°	$2^\circ/52^\circ$	111°	-/4.15/-	-	-	6.1
Yao et al. (2020)	77.86°	39.31°	269°	20°	92°	4/5/6	58/30	2.29×10^{18}	6.2
He et al. (2021)	77.45°	39.79°	276°	10.2°	109°	5/7.3/9.6	50/26	$- \times 10^{18}$	6.08

369 the upper row shows waveforms with the depth fixed to match the geodetic results at 7 km, and the
 370 lower row shows waveforms with the depth fixed to match the centre of the regionally-determine
 371 aftershock distribution at 15 km. We discuss these waveform misfits further in the following sec-
 372 tion.

373 5 DISCUSSION

374 5.1 Depth discrepancy between the 2020 Jiashi mainshock and its aftershocks

375 Our InSAR-derived model suggests that the Jiashi mainshock ruptured along the décollement
 376 at the base of the sedimentary cover, with a centroid depth of ~ 7 km. From the high-quality
 377 locally-recorded and double-difference relocated aftershock data, aftershocks cluster along E–W
 378 and NNW–SSE trends, with the former matching the ~ 40 km length and orientation of our slip
 379 model (Supplementary Figs. S12 and S13) (Ran et al., 2020; Yao et al., 2021a; He et al., 2021).
 380 However, locally-recorded aftershocks concentrate at 10–20 km depth, well below the depth of

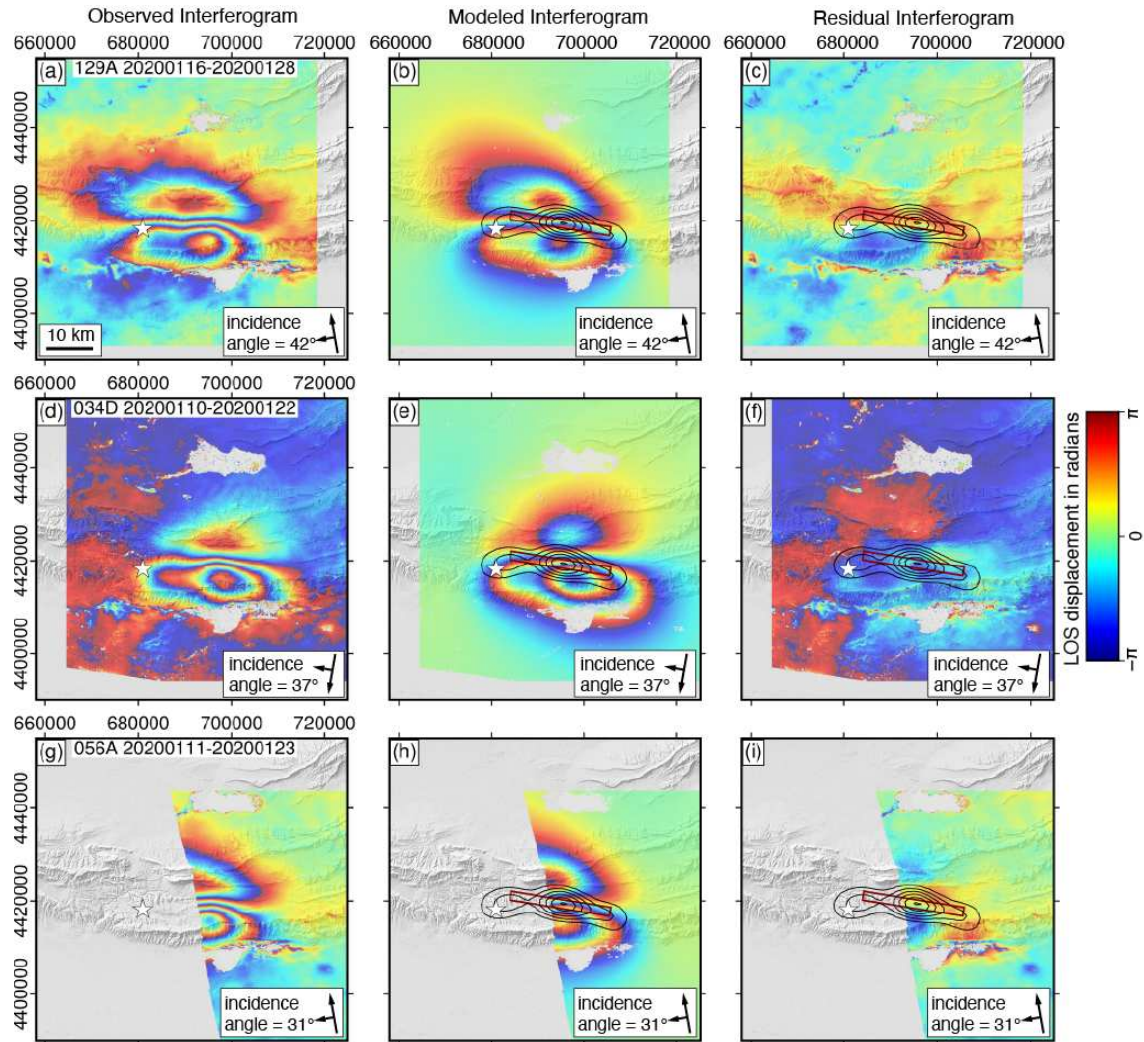


Figure 2. (Left column) Observed, (center) distributed slip model and (right) residual interferograms of the 2020 Jiashi mainshock rupture. Modelling was performed using unwrapped LOS displacements, but here we plot the original, wrapped (filtered) interferograms since these show more clearly the shape of the deformation field. The coordinates are in UTM 43N. Color cycles of blue through yellow to red indicate motion away from the satellite and one color cycle (2π radians) represents a half radar wavelength (2.8 cm) of LOS displacement. The satellite track azimuths and LOS direction with local angle of incidence are indicated by the longer and shorter black arrows, respectively. The white star indicates the relocated mainshock epicenter. In the central and right-hand panels, ten centimeter model slip contours are shown in black and the outline of the uniform slip model fault plane is marked in dark red.

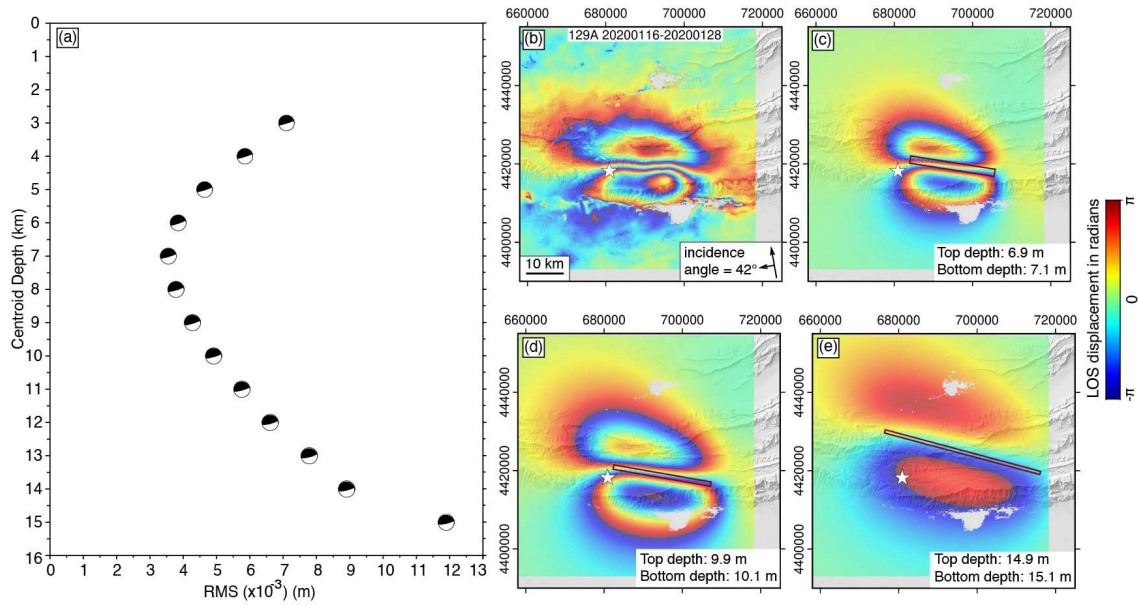


Figure 3. (a) Fault center depth sensitivity tests of our InSAR uniform slip fault models for the 2020 Jiashi mainshock. Each focal mechanism shows the minimum-misfit model solution for a fixed center depth, with all other parameters kept free in each inversion. The x -axis is root mean square error (RMS) in meters; the y axis shows 1 km increments of fixed center depth. (b) Observed ascending track interferogram (same as in Fig. 2a). (c) Preferred uniform slip model interferogram, with its (free) center depth of 7 km. (d) A forward model interferogram with center depth fixed to 10 km. The forward model used the same uniform slip parameters as in (c) except for the top and bottom depth and the surface projection coordinates. (e) Same as (d) but with a centroid depth of 15 km. The coordinates are in UTM 43N.

381 mainshock slip resolved by InSAR inversion. We consider two possible explanations for this ap-
 382 parent discrepancy.

383 The first possible explanation is that the surface deformation captured with InSAR may reflect
 384 aseismic afterslip along the décollement, above an earthquake buried within the underlying base-
 385 ment (at the depth of the aftershock concentration) and itself invisible to InSAR. We tested this
 386 possibility by forward modelling the interferograms based upon a M_w 6.0 thrust earthquake with
 387 the same geometry as our preferred uniform slip model fault but centered at depths of 10 km and
 388 15 km, more consistent with the aftershock seismicity (Fig. 3c, d). These forward model interfer-

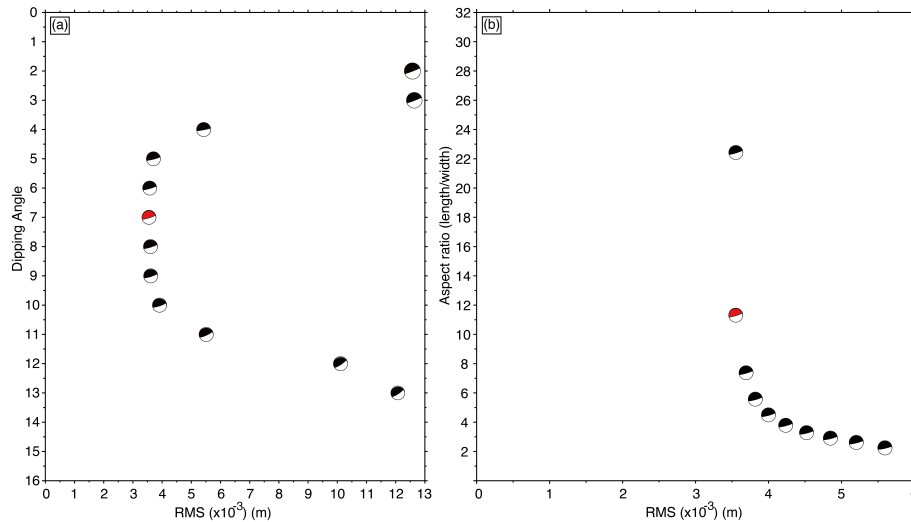


Figure 4. (a) Fault dip sensitivity tests of our InSAR uniform slip fault models for the 2020 Jiashi mainshock. Each focal mechanism shows the minimum-misfit model solution for a fixed dip angle, with all other parameters kept free in each inversion. The x -axis is root mean square error (RMS) in meters; the y axis shows 1° increments of fixed dip. The one with red compression part indicates the optimal uniform slip model. (b) Fault plane width sensitivity tests. Each focal mechanism shows the minimum-misfit model solution for a fixed fault width (obtained by fixing the centroid depth and dip to the minimum misfit values and extending the fault plane up- and down-dip at 1 kilometer increments). All other parameters, including slip and fault length, are allowed to vary and the results are plotted according to the aspect ratio of length to width. The red focal mechanism indicates the optimal uniform slip model.

389 ograms match poorly with the observed InSAR data, with noticeably more far-field deformation
 390 and a broader spacing of fringes between the southern and northern lobes. However, the fact that
 391 this surface deformation remains distinguishable leads us to rule out the possibility that coseismic
 392 slip is too deep to be resolved with InSAR.

393 The second possible explanation is that the InSAR captures mainshock slip but that well-
 394 located aftershocks are vertically separated from the mainshock within the underlying basement,
 395 perhaps concentrated within a lobe of positive Coulomb stress change expected below the base
 396 of a thrust or reverse fault (e.g. Lin & Stein, 2004; Zhou et al., 2019). He et al. (2021) showed
 397 that double-difference relocated aftershocks concentrate along two steep planes within the base-
 398 ment; they then used Coulomb stress calculations to estimate the kinematics of these faults most

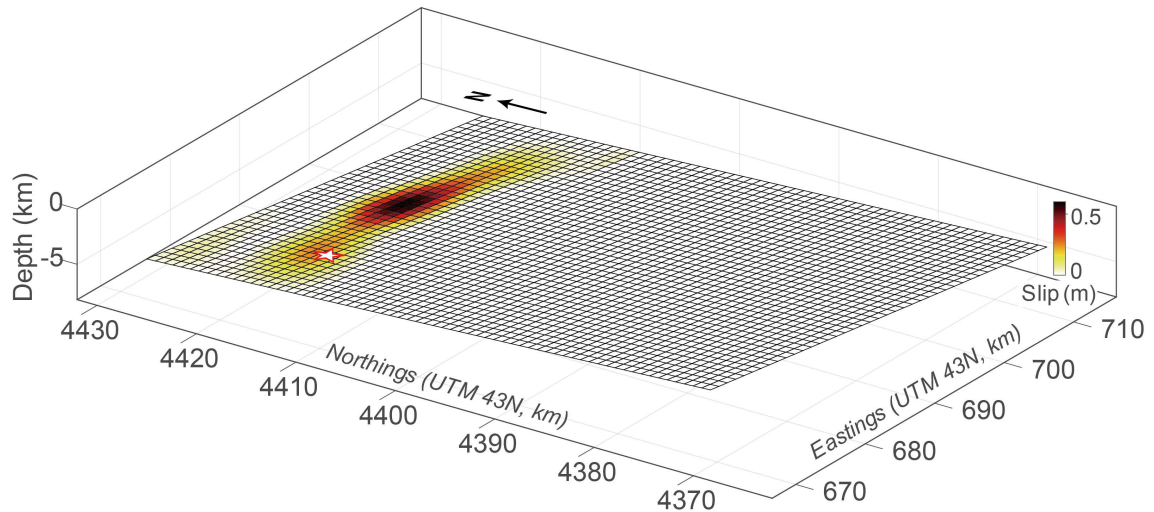


Figure 5. The perspective view of the coseismic slip distribution. The fault plane dips to north shallowly. Significant slip occurs over the depth range 6.5–7.4 km. The red star marks the relocated epicenter near the western end of the deformation field for the 2020 Jiashi earthquake.

399 consistent with static stress triggering by the shallower mainshock. This implies that the basement
 400 aftershocks involved N–S-oriented sinistral and steep, S-dipping reverse faulting. However, this
 401 does not explain the absence of shallow aftershocks within positive Coulomb stress lobes expected
 402 above the top mainshock fault edge. This might reflect an effect on the stress field from the stress-
 403 free boundary of the Earth’s surface, that the faults within the sediments above the décollement
 404 may exhibit velocity-strengthening friction, favouring aseismic creep over seismic slip (Karasözen
 405 et al., 2016), or that the seismic network is insensitive to shallow events due to its average station
 406 spacing of ~ 30 km. Local seismic networks are able to constrain the focal depth most accurately
 407 only if P_g and S_g phases are recorded at epicentral distances of less than ~ 1 – 2 times of focal
 408 depths and the average station spacing is also less than ~ 1 – 2 times of focal depths (Gomberg
 409 et al., 1990). Therefore, the apparent absence of shallow events may be an artefact, as the stations
 410 with average spacing of ~ 30 km cannot record aftershocks shallower than 15 km depth.

411 We agree with the explanation favored by He et al. (2021) that the mainshock and aftershocks
 412 are vertically separated, as our teleseismic waveform inversion reinforces that the geodetically-

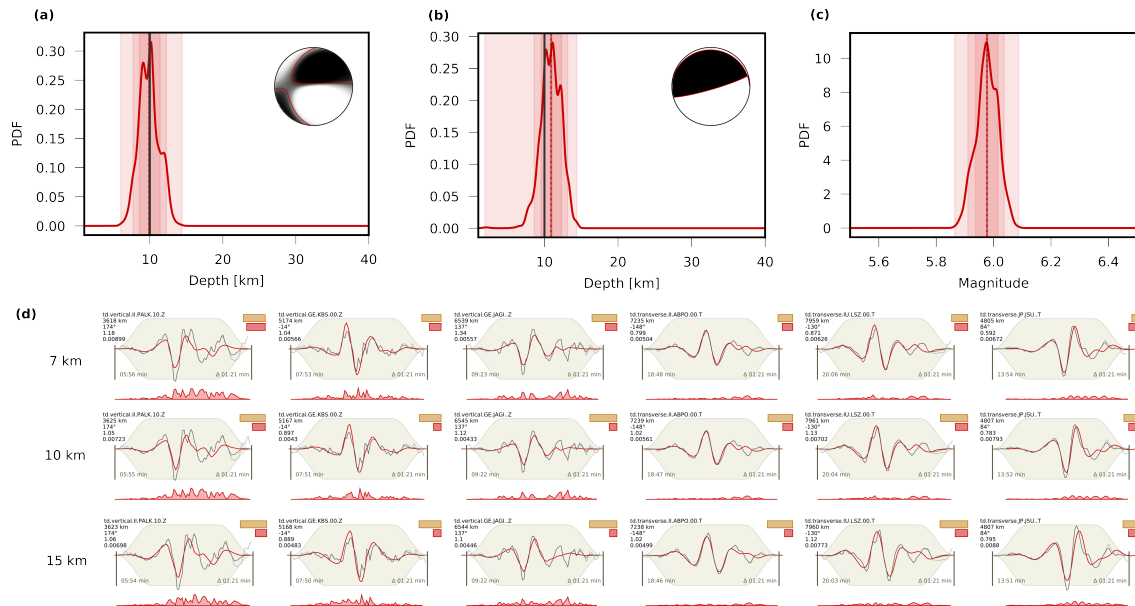


Figure 6. Seismological processing results for the 2020 Jiashi mainshock. (a) Probability-density function for depth, for an inversion with all parameters free. Inset mechanism shows the mechanism probability density function (greys) and the best-fit solution (red). (b) Probability-density function for depth, for an inversion with the mechanism constrained to be a double couple matching the InSAR-derived fault plane. (c) Probability-density function for moment, for an inversion with the mechanism constrained to match the InSAR-derived fault plane. (d) Example waveforms for 6 stations (three vertical component, three transverse component). Black traces show the observed data, red line shows the best-fitting inversion result. Text on each waveform indicates the station and component, epicentral distance, and azimuth. Each row of waveforms show synthetics calculated at 7, 10, and 15 km respectively, as discussed in the text.

413 imaged signal is indeed coseismic. The waveform misfit differences between depths of 10 km and
 414 7 km are minimal (Fig. 6d). However, synthetics are notably too broad at all six of the stations
 415 shown when the depth is increased to 15 km. Due to the cross-correlation based alignment, syn-
 416 thetics are typically aligned on the dominant peak to minimise misfit. However, at 15 km depth,
 417 this leads to the peaks to either side being too far out from the main peak due to the increase
 418 separation between direct and depth phases. Thus, we conclude that the seismological data are
 419 consistent with the deformation signal detected using InSAR, but are notably shallower than the
 420 aftershocks located using regional seismology.

421 Mainshock–aftershock depth discrepancies are not uncommon and several other earthquake
422 sequences also exhibit similar characteristics. The 2000 M_w 6.6 Torrori (Japan), 2003 M_w 6.6
423 Bam (Iran), 2008 M_w 7.9 Wenchuan (China), 2009 M_w 5.9 Karonga (Malawi), 2011 M_w 5.9
424 Simav (Turkey), and 2014 M_w 6.1 South Napa (California) earthquakes all exhibited shallower
425 mainshock slip, resolved mostly using geodesy, with deeper aftershock distributions, resolved us-
426 ing seismology (Semmane et al., 2005; Jackson et al., 2006; Tong et al., 2010; Wei et al., 2015;
427 Karasözen et al., 2016; Gaherty et al., 2019). Similar patterns were also observed in $M_w \sim 6$ earth-
428 quakes and aftershock sequences at Qeshm (2005) and Fin (2006) in the Zagros Simply Folded
429 Belt, Iran (Nissen et al., 2010; Roustaei et al., 2010). These are especially analogous to the Jiashi
430 sequence, as the Zagros mainshocks were centered within a thick sedimentary cover, with after-
431 shock microseismicity vertically separated within the underlying basement (Nissen et al., 2014).
432 Finally, we recollect that the February 24, 2003 M_w 6.2 Jiashi earthquake in the foreland basin
433 south of the Kepingtag was centered at $\sim 5\text{--}7$ km depth, but exhibited aftershocks at $\sim 15\text{--}25$ km
434 depth (Huang et al., 2006; Sloan et al., 2011).

435 **5.2 Structural interpretation of the 2020 Jiashi rupture**

436 Coseismic uplift in the 2020 M_w 6.0 Jiashi earthquake resolved by InSAR is centered along the
437 back limb of the Kepingtag anticline (Fig. 7a–d). Seismic reflection profiles and balanced geologi-
438 cal cross-sections depict this as a fault-propagation fold, with Paleozoic-Mesozoic sediments thrust
439 over Cenozoic strata along the moderately northward-dipping Kepingtag fault, which branches off
440 a décollement with an estimated depth of $\sim 5\text{--}10$ km (Yin et al., 1998; Allen et al., 1999; Yang
441 et al., 2010, 2002). Projecting our slip model onto a modified geological cross-section suggests that
442 the 2020 earthquake ruptured the décollement where it intersects with the base of the Kepingtag
443 thrust fault (Fig. 7e).

444 A striking feature of our distributed slip model is its elongate shape, with a length-to-width
445 aspect ratio of greater than 4 (Fig. 5). This indicates that the earthquake was able to propagate
446 readily along strike, but was prevented from doing so up- and down-dip. We consider two potential
447 causes of this pattern. One possibility is that the stratigraphic configuration could have determined

448 where slip was able to propagate, with rupture restricted to competent rocks such as the lowermost
449 Cambrian limestone. A similar explanation was proposed by Elliott et al. (2015) for the elongate
450 slip distribution (length-to-width ratio ~ 3) of the 2013 M_w 6.2 Khaki-Shonbe earthquake in the
451 Zagros fold-and-thrust belt, where Infracambrian Hormuz evaporites and Cretaceous Kazhdumi
452 mudstones were inferred to have controlled the bottom and top of the rupture, respectively. Length-
453 to-width ratios of ~ 3 –4 inferred for the 2006 Fin and 2019 Khalili earthquakes (both M_w 5.7)
454 suggest that this may be a common feature of Zagros ruptures (Roustaei et al., 2010; Jamalreyhani
455 et al., 2021). Another possible mechanism could be due to structural complexities in the fault
456 geometry. This was discussed by Elliott et al. (2011) for the 2008 and 2009 Qaidam M_w 6.3
457 earthquakes, whose vertical segregation resulted from disruption of the rupture plane by a cross-
458 cutting, conjugate reverse fault. In the 2020 Jiashi event, we suggest that the abrupt change in
459 dip angle between the sub-horizontal décollement and the much steeper Kepingtag fault may have
460 provided a barrier to rupture. Our testing of listric fault geometries is in good agreement with the
461 inference that there was minimal slip on the steeper fault. Although the current data does not allow
462 us to distinguish between the two mechanisms, there is a clear structural or lithological control on
463 the extent of coseismic slip during the mainshock.

464 **5.3 Regional distribution of seismicity and seismic hazard**

465 The Pamir and Tian Shan jointly accommodate a crustal shortening of 20–25 mm/yr, nearly half
466 of the total India-Eurasia convergence rate (Abdrakhmatov et al., 1996; Zubovich et al., 2010).
467 The southwestern margin of the Tian Shan is characterized by frequent seismicity, mostly with
468 thrust faulting and strike-slip mechanisms. Here, we use our own calibrated earthquake reloca-
469 tions together with previous waveform modelling studies to assess the finer-scale distribution of
470 seismicity across this region.

471 From the calibrated earthquake relocations, it is apparent that seismicity is not concentrated
472 along the frontal Kepingtag belt, but is distributed throughout the fold-and-thrust belt as well as
473 the adjacent foreland to the south. The shallow events occur to the north of the frontal Kepingtag
474 anticline as well as in the foreland to the south. This pattern indicates that all stacks of the thrust

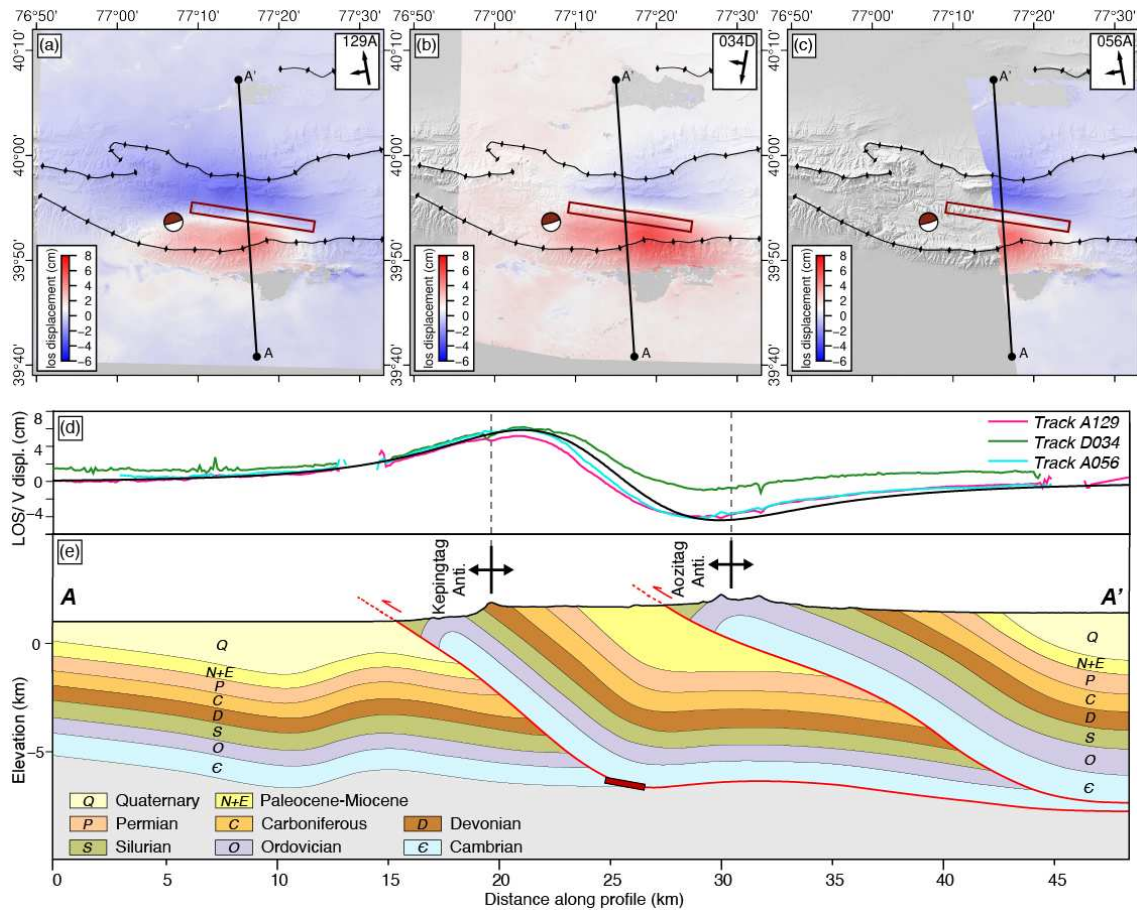


Figure 7. Coseismic LOS displacements in the 2020 Jiashi earthquake from unwrapped interferograms on tracks (a) 129A, (b) 034D and (c) 056A. Black lines with ticks show the traces of the Aozitang (north) and Kepingtag (south) fold axes. The dark red rectangle is the uniform slip model fault plane, centered at ~ 7 km depth. (d) LOS displacement profiles and vertical displacement profile (track A129 in pink, D034 in green, A056 in cyan, and vertical displacement in black) along profile A-A' in (a), (b) and (c). Maximum LOS displacements are ~ 7.5 cm toward the satellite and ~ 4 cm away from the satellite. Vertical displacement field is predicted by our best fitting, InSAR-derived distributed slip model. (e) Geological cross-section along the profile A-A', interpreted from seismic reflection profiles (Yang et al., 2010). The surface topography is extracted from the 30 m resolution SRTM DEM. The dark red rectangle indicates the uniform slip model fault plane.

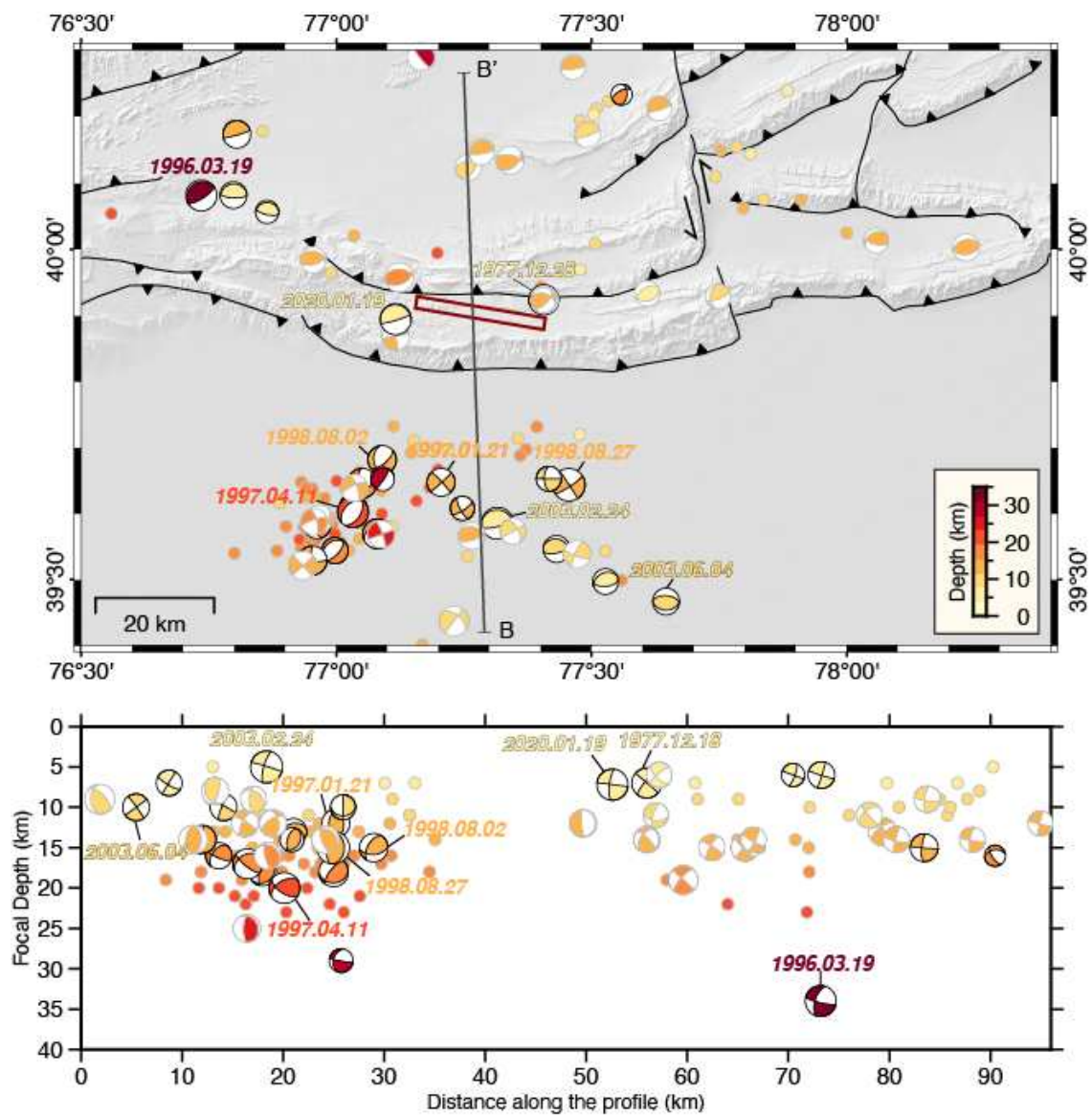


Figure 8. Calibrated relocated earthquakes from 1977–2020 in the Jiashi area, coloured according to the best available estimate of depth. Focal mechanisms determined by teleseismic and regional waveform modelling, including some from the GCMT catalogue. The depths of focal mechanisms with black outlines are determined by teleseismic and regional waveform modelling and depth phases, while those with grey outlines are our own calibrated focal depths (see Table 2 for full details). Other moderate relocated earthquakes without focal mechanisms are shown as dots.

475 sheets may be simultaneously capable of generating earthquakes, even as one of them might be
476 most favourable at a particular time due to a variable stress state and the history of previous earth-
477 quakes. This inference is also supported by geomorphological and geochronological data (Yang
478 et al., 2006) and suggests that seismic hazard is high across the region, rather than being focused
479 along the range front.

480 Moreover, the seismic hazard in the Kepingtag region is not only restricted to faulting along
481 the décollement but also within the folded cover rocks and the piedmont area. Reliable earthquake
482 centroid and focal depths — from teleseismic or regional waveform modelling (Fan et al., 1994;
483 Ghose et al., 1998; Sloan et al., 2011) and our own calibrated hypocentral relocations — are
484 concentrated at depths shallower than 25 km, except for two isolated events at 29–35 km (Fig. 8).
485 The 1997 Jiashi earthquake swarm and the 2003 Bachu-Jiashi sequence all occurred on blind faults
486 in the piedmont area ~50 km south of the Kepingtag frontal thrust. The largest events between
487 1997 and 1998 (M_w 5.7, 5.9, 6.0 and 6.3) represented activity on normal faulting or left-lateral
488 strike-slip faulting at mid-crustal depths of ~12–20 km, while the 2003 events involved much
489 shallower thrust faulting (Sloan et al., 2011). Within the Kepingtag fold-and-thrust belt, most of
490 the reliable centroid depths are greater than 10 km, indicating faulting within the basement is below
491 the décollement. Though usually depicted as a ‘thin-skinned’ fold-and-thrust belt, the Kepingtag
492 basement clearly accommodates shortening by reverse faulting, and should therefore be considered
493 as an important source of seismic hazard.

494 **6 CONCLUSION**

495 We use InSAR data to characterize the coseismic surface deformation and model the fault geom-
496 etry and slip distribution of the January 19 2020 M_w 6.0 Jiashi earthquake. Modelled coseismic
497 uplift is centered on the back limb of the Kepingtag anticline, consistent with previous structural
498 models that depict this as a fault-propagation fold. Our best-fit model fault plane dips ~7° north-
499 ward at depth of ~7 km, placing it on or close to the mapped décollement at the base of the folded
500 sedimentary cover. This depth is consistent with teleseismic body-waveforms, confirming that the
501 slip modelled with InSAR occurred coseismically. The small (~1/4) width to length ratio of our

502 model slip distribution hints at structural and/or lithological controls on slip propagation; for ex-
503 ample, rupture may have been prevented from advancing up-dip by the abrupt change of dip angle
504 between the sub-horizontal décollement and the much steeper Kepingtag thrust. Published seis-
505 mological studies show that aftershocks cluster within underlying basement rocks at $\sim 10\text{--}20$ km
506 depth, vertically separated from the mainshock slip. Our own relocated background seismicity
507 also shows a prevalence of seismicity at basement depths throughout the Kepingtag belt and its
508 foreland, hinting at rheological controls on the depths at which earthquakes occur.

509 **ACKNOWLEDGMENTS**

510 S. W. was supported by the China Scholarship Council and a Graduate Award from University of
511 Victoria. E. N. and R. J. were funded separately by the Natural Science and Engineering Research
512 Council of Canada (NSERC), the Canada Foundation for Innovation (CFI) and the BC Knowledge
513 Development Fund (BCKDF). E. N. also acknowledges support from a Canada Research Chair.
514 T. C. was supported by the Royal Society (UK) under URF\R1\180088. T. C. was also supported
515 through COMET, the UK Natural Environment Research Council's Centre for the Observation and
516 Modelling of Earthquakes, Volcanoes, and Tectonics. We are grateful to two anonymous reviewers
517 for their constructive comments which significantly improve the manuscript.

518 **Data availability**

519 Interferograms were constructed using Copernicus Sentinel-1 data (2020) available from <https://scihub.coperni>
520 and processed in GAMMA software (<https://www.gamma-rs.ch/>). InSAR modelling codes are
521 available from E. N. upon request. Earthquakes were relocated using *Mloc* software (<https://seismo.com/mloc/>)
522 using starting location parameters from the International Seismological Centre Bulletin (<http://www.isc.ac.uk/is>)
523 Full calibrated relocation results will be posted to the USGS ScienceBase website for the Global
524 Catalog of Calibrated Earthquake Locations (GCCEL) ([https://www.sciencebase.gov/catalog/item/](https://www.sciencebase.gov/catalog/item/59fb91fde4b0531197b16ac7)
525 [59fb91fde4b0531197b16ac7](https://www.sciencebase.gov/catalog/item/59fb91fde4b0531197b16ac7)). We also used focal mechanism data from the Global Centroid Mo-
526 ment Tensor project (<https://www.globalcmt.org/>). Several of the figures in the paper were plotted
527 using Generic Mapping Tools (Wessel et al., 2019).

528 **References**

- 529 Abdrakhmatov, K. Y., Aldazhanov, S. A., Hager, B. H., Hamburger, M. W., Herring, T. A., Kal-
530 abaev, K. B., Makarov, V. I., Molnar, P., Panasyuk, S. V., Prilepin, M. T., Reilinger, R. E.,
531 Sadybakasov, I. S., Souter, B. J., Trapeznikov, Y. A., Tsurkov, V. Y., & Zubovich, A. V., 1996.
532 Relatively recent construction of the Tien Shan inferred from GPS measurements of present-day
533 crustal deformation rates, *Nature*, **384**(6608), 450–453.
- 534 Ainscoe, E. A., Elliott, J. R., Copley, A., Craig, T. J., Li, T., Parsons, B. E., & Walker, R. T., 2017.
535 Blind Thrusting, Surface Folding, and the Development of Geological Structure in the Mw 6.3
536 2015 Pishan (China) Earthquake, *Journal of Geophysical Research: Solid Earth*, **122**(11), 9359–
537 9382.
- 538 Allen, M. B., Vincent, S. J., & Wheeler, P. J., 1999. Late Cenozoic tectonics of the Kepingtage
539 thrust zone: Interactions of the Tien Shan and Tarim Basin, northwest China, *Tectonics*, **18**(4),
540 639–654.
- 541 Avouac, J. P. & Tapponnier, P., 1993. Kinematic model of active deformation in central Asia,
542 *Geophysical Research Letters*, **20**(10)(10), 895–898.
- 543 Bayasgalan, A., Jackson, J., & McKenzie, D., 2005. Lithosphere rheology and active tectonics
544 in mongolia: relations between earthquake source parameters, gravity and gps measurements,
545 *Geophysical Journal International*, **163**(3), 1151–1179.
- 546 Beckers, J. & Lay, T., 1995. Very broadband seismic analysis of the 1992 Flores, Indonesia,
547 earthquake ($M_w = 7.9$), *Journal of Geophysical Research: Solid Earth*, **100**(B9), 18,179–18,193.
- 548 Bergman, E. A., Benz, H. M., Yeck, W. L., Karasözen, E., Engdahl, E. R., Ghods, A., Hayes, G. P.,
549 & Earle, P. S., submitted. A Global Catalog of Calibrated Earthquake Locations, *Geophysical*
550 *Journal International*.
- 551 Bie, L., Ryder, I., Nippress, S. E. J., & Bürgmann, R., 2014. Coseismic and post-seismic activity
552 associated with the 2008 M_w 6.3 Damxung earthquake, Tibet, constrained by InSAR, *Geophys-*
553 *ical Journal International*, **196**(2), 788–803.
- 554 Bro, R. & De Jong, S., 1997. A fast non-negativity-constrained least squares algorithm, *Journal*
555 *of Chemometrics*, **11**(5), 393–401.

- 556 Burchfiel, B. C., Brown, E. T., Qidong, D., Xianyue, F., Jun, L., Molnar, P., Jianbang, S., Zhang-
557 ming, W., & Huichuan, Y., 1999. Crustal shortening on the margins of the tien shan, Xinjiang,
558 China, *International Geology Review*, **41**(8), 665–700.
- 559 Chen, J., Ran, Y., Yang, X., & Xu, X., 2006. Character of Late Quaternary activity of the east
560 segment of the front-edge faults of Kalpintag, *Seismology and Geology*, **28**(2), 258–268 (in
561 Chinese with English abstract).
- 562 Chounet, A., Vallée, M., Causse, M., & Courboulex, F., 2018. Global catalog of earthquake rup-
563 ture velocities shows anticorrelation between stress drop and rupture velocity, *Tectonophysics*,
564 **733**, 148–158.
- 565 Copley, A., 2014. Postseismic afterslip 30 years after the 1978 Tabas-e-Golshan (Iran) earth-
566 quake: observations and implications for the geological evolution of thrust belts, *Geophysical*
567 *Journal International*, **197**(2), 665–679.
- 568 Copley, A., Karasozen, E., Oveisi, B., Elliott, J. R., Samsonov, S., & Nissen, E., 2015. Seis-
569 mogenic faulting of the sedimentary sequence and laterally variable material properties in the
570 Zagros Mountains (Iran) revealed by the August 2014 Murmuri (E. Dehloran) earthquake se-
571 quence, *Geophysical Journal International*, **203**(2), 1436–1459.
- 572 Davis, T. L., Namson, J., & Yerkes, R. F., 1989. A cross section of the Los Angeles area: seismi-
573 cally active fold and thrust belt, the 1987 Whittier Narrows earthquake, and earthquake hazard,
574 *Journal of Geophysical Research*, **94**(B7), 9644–9664.
- 575 Elliott, J. R., Parsons, B., Jackson, J. A., Shan, X., Sloan, R. A., & Walker, R. T., 2011. Depth
576 segmentation of the seismogenic continental crust: The 2008 and 2009 Qaidam earthquakes,
577 *Geophysical Research Letters*, **38**(6), 1–6.
- 578 Elliott, J. R., Copley, A. C., Holley, R., Scharer, K., & Parsons, B., 2013. The 2011 Mw 7.1 Van
579 (Eastern Turkey) earthquake, *Journal of Geophysical Research (Solid Earth)*, **118**(4), 1619–
580 1637.
- 581 Elliott, J. R., Bergman, E. A., Copley, A. C., Ghods, A. R., Nissen, E. K., Oveisi, B., Tatar, M.,
582 Walters, R. J., & Yamini-Fard, F., 2015. The 2013 Mw 6.2 Khaki-Shonbe (Iran) Earthquake:
583 Insights into seismic and aseismic shortening of the Zagros sedimentary cover, *Earth and Space*

584 *Science*, **2**(11), 435–471.

585 Elliott, J. R., Walters, R. J., & Wright, T. J., 2016. The role of space-based observation in un-
586 derstanding and responding to active tectonics and earthquakes, *Nature Communications*, **7**,
587 13844.

588 Engdahl, R. E., Jackson, J. A., Myers, S. C., Bergman, E. A., & Priestley, K., 2006. Relocation
589 and assessment of seismicity in the Iran region, *Geophysical Journal International*, **167**(2),
590 761–778.

591 Fan, G., Ni, J. F., & Wallace, T. C., 1994. Active tectonics of the Pamirs and Karakorum, *Journal*
592 *of Geophysical Research*, **99**(B4), 7131.

593 Funning, G. J., Parsons, B., Wright, T. J., Jackson, J. A., & Fielding, E. J., 2005. Surface displace-
594 ments and source parameters of the 2003 Bam (Iran) earthquake from Envisat advanced syn-
595 thetic aperture radar imagery, *Journal of Geophysical Research: Solid Earth*, **110**(B9), B09406.

596 Gaherty, J. B., Zheng, W., Shillington, D. J., Pritchard, M. E., Henderson, S. T., Chindandali,
597 P. R., Mdala, H., Shuler, A., Lindsey, N., Oliva, S. J., Nooner, S., Scholz, C. A., Schaff, D.,
598 Ekström, G., & Nettles, M., 2019. Faulting processes during early-stage rifting: Seismic and
599 geodetic analysis of the 2009-2010 Northern Malawi earthquake sequence, *Geophysical Journal*
600 *International*, **217**(3), 1767–1782.

601 Gao, R., Hou, H., Cai, X., Knapp, J. H., He, R., Liu, J., Xiong, X., Guan, Y., Li, W., Zeng, L.,
602 & Roecker, S. W., 2013. Fine crustal structure beneath the junction of the southwest Tian Shan
603 and Tarim Basin, NW China, *Lithosphere*, **5**(4), 382–392.

604 Gaudreau, É., Nissen, E., Bergman, E. A., Benz, H. M., Tan, F., & Karasözen, E., 2019. The Au-
605 gust 2018 Kaktovik earthquakes: Active tectonics in northeastern Alaska revealed with InSAR
606 and seismology, *Geophysical Research Letters*, **46**(24), 14412–14420.

607 Ghose, S., Hamburger, M. W., & Ammon, C. J., 1998. Source parameters of moderate-sized
608 earthquakes in the Tien Shan, central Asia from regional moment tensor inversion, *Geophysical*
609 *Research Letters*, **25**(16), 3181–3184.

610 Goldstein, R. M., Zebker, H. A., & Werner, C. L., 1988. Satellite radar interferometry: Two-
611 dimensional phase unwrapping, *Radio Science*, **23**(4), 713–720.

- 612 Gomberg, J. S., Shedlock, K. M., & Roecker, S. W., 1990. The effect of S-wave arrival times
613 on the accuracy of hypocenter estimation, *Bulletin of the Seismological Society of America*,
614 **80**(6A), 1605–1628.
- 615 He, Y., Wang, T., Fang, L., & Zhao, L., 2021. The 2020 Mw 6.0 Jiashi Earthquake: Coin-
616 volvement of Thin-Skinned Thrusting and Basement Shortening in Shaping the Keping-Tage
617 Fold-and-Thrust Belt in Southwestern Tian Shan, *Seismological Research Letters*.
- 618 Heimann, S., Isken, M., Kühn, D., Sudhaus, H., Steinberg, A., Daout, S., Cesca, S., Bathke, H.,
619 & Dahm, T., 2018. Grond: A probabilistic earthquake source inversion framework.
- 620 Hendrix, M. S., Graham, S. A., Carroll, A. R., Sobel, E. R., McKnight, C. L., Schulein, B. J., &
621 Wang, Z., 1992. Sedimentary record and climatic implications of recurrent deformation in the
622 Tian Shan: evidence from Mesozoic strata of the north Tarim, south Junggar, and Turpan basins,
623 northwest China, *Geological Society of America Bulletin*, **104**(1), 53–79.
- 624 Huang, Y., Yang, J. S., & Zhang, T. Z., 2006. Relocation of the Bachu-Jiashi, Xinjiang earthquake
625 sequence in 2003 using the double-difference location algorithm, *Acta Geophysica Sinica*,
626 **49**(1), 162–169.
- 627 Jackson, J., Bouchon, M., Fielding, E., Funning, G., Ghorashi, M., Hatzfeld, D., Nazari, H., Par-
628 sons, B., Priestley, K., Talebian, M., Tatar, M., Walker, R., & Wright, T., 2006. Seismotectonic,
629 rupture process, and earthquake-hazard aspects of the 2003 December 26 Bam, Iran, earthquake,
630 *Geophysical Journal International*, **166**(3), 1270–1292.
- 631 Jamalreyhani, M., Pousse-Beltran, L., Büyükakpınar, P., Cesca, S., Nissen, E., Ghods, A., López-
632 Comino, J. Á., Rezapour, M., & Najafi, M., 2021. The 2019-2020 Khalili (Iran) Earthquake Se-
633 quence—Anthropogenic Seismicity in the Zagros Simply Folded Belt?, *Journal of Geophysical*
634 *Research (Solid Earth)*, **126**(12), e22797.
- 635 Jones, L., Aki, K., Boore, D., Celebi, M., Donnellan, A., Hall, J., Harris, R., Hauksson, E.,
636 Heaton, T., Hough, S., Hudnut, K., Hutton, K., Johnston, M., Joyner, W., Kanamori, H., Mar-
637 shall, G., Michael, A., Mori, J., Murray, M., Ponti, D., Reasenber, P., Schwartz, D., Seeber,
638 L., Shakal, A., Simpson, R., Thio, H., Tinsley, J., Todorovska, M., Trifunac, M., Wald, D., &
639 Zoback, M. L., 1994. The magnitude 6.7 Northridge, California, earthquake of 17 January 1994,

- 640 *Science*, **266**(5184), 389–397.
- 641 Jónsson, S., Zebker, H., Segall, P., & Amelung, F., 2002. Fault slip distribution of the 1999 Mw
642 7.1 Hector Mine, California, earthquake, estimated from satellite radar and GPS measurements,
643 *Bulletin of the Seismological Society of America*, **92**(4), 1377–1389.
- 644 Jordan, T. H. & Sverdrup, K. A., 1981. Teleseismic location techniques and their application to
645 earthquake clusters in the South-Central Pacific, *Bulletin of the Seismological Society of Amer-*
646 *ica*, **71**, 1105–1130.
- 647 Karasözen, E., Nissen, E., Bergman, E. A., Johnson, K. L., & Walters, R. J., 2016. Normal fault-
648 ing in the Simav graben of western Turkey reassessed with calibrated earthquake relocations,
649 *Journal of Geophysical Research: Solid Earth*, **121**(6), 4553–4574.
- 650 Karasözen, E., Nissen, E., Büyükakpınar, P., Cambaz, M. D., Kahraman, M., Kalkan & Ertan,
651 E., Abgarmi, B., Bergman, E., Ghods, A., & Özacar, A. A., 2018. The 2017 July 20 M_w 6.6
652 Bodrum-Kos earthquake illuminates active faulting in the Gulf of Gökova, SW Turkey, *Geo-*
653 *physical Journal International*, **214**(1), 185–199.
- 654 Karasözen, E., Nissen, E., Bergman, E. A., & Ghods, A., 2019. Seismotectonics of the Za-
655 gros (Iran) From Orogen-Wide, Calibrated Earthquake Relocations, *Journal of Geophysical Re-*
656 *search: Solid Earth*, **124**(8), 9109–9129.
- 657 Kennett, B. L. N., Engdahl, E. R., & Buland, R., 1995. Constraints on seismic velocities in the
658 Earth from traveltimes, *Geophysical Journal International*, **122**(1), 108–124.
- 659 Kulikova, G. & Krüger, F., 2017. Historical seismogram reproductions for the source parameters
660 determination of the 1902, Atushi (Kashgar) earthquake, *Journal of Seismology*, **21**(6), 1577–
661 1597.
- 662 Li, S. & Barnhart, W. D., 2020. Impacts of Topographic Relief and Crustal Heterogeneity on Co-
663 seismic Deformation and Inversions for Fault Geometry and Slip: A Case Study of the 2015
664 Gorkha Earthquake in the Central Himalayan Arc, *Geochemistry, Geophysics, Geosystems*,
665 **21**(12), e09413.
- 666 Lin, J. & Stein, R. S., 2004. Stress triggering in thrust and subduction earthquakes and stress
667 interaction between the southern San Andreas and nearby thrust and strike-slip faults, *Journal*

- 668 *of Geophysical Research (Solid Earth)*, **109**(B2), B02303.
- 669 Mallick, R., Bürgmann, R., Johnson, K., & Hubbard, J., 2021. A unified framework for earth-
670 quake sequences and the growth of geological structure in fold-thrust belts, *Journal of Geophys-*
671 *ical Research: Solid Earth*.
- 672 Nishidai, T. & Berry, J. L., 1990. Structure and Hydrocarbon Potential of the Tarim Basin (Nw
673 China) From Satellite Imagery, *Journal of Petroleum Geology*, **13**(1), 35–58.
- 674 Nissen, E., Ghorashi, M., Jackson, J., Parsons, B., & Talebian, M., 2007. The 2005 Qeshm Island
675 earthquake (Iran) - A link between buried reverse faulting and surface folding in the Zagros
676 Simply Folded Belt?, *Geophysical Journal International*, **171**(1), 326–338.
- 677 Nissen, E., Yamini-Fard, F., Tatar, M., Gholamzadeh, A., Bergman, E., Elliott, J. R., Jackson,
678 J. A., & Parsons, B., 2010. The vertical separation of mainshock rupture and microseismicity
679 at Qeshm island in the Zagros fold-and-thrust belt, Iran, *Earth and Planetary Science Letters*,
680 **296**(3-4), 181–194.
- 681 Nissen, E., Tatar, M., Jackson, J. A., & Allen, M. B., 2011. New views on earthquake faulting in
682 the Zagros fold-and-thrust belt of Iran, *Geophysical Journal International*, **186**(3), 928–944.
- 683 Nissen, E., Jackson, J., Jahani, S., & Tatar, M., 2014. Zagros "phantom earthquakes" reassessed -
684 The interplay of seismicity and deep salt flow in the Simply Folded Belt?, *Journal of Geophys-*
685 *ical Research: Solid Earth*, **119**(4), 3561–3583.
- 686 Okada, Y., 1985. Surface deformation due to shear and tensile faults in a half-space, *Bulletin of*
687 *the seismological society of America*, **75**(4), 1135–1154.
- 688 Pousse-Beltran, L., Nissen, E., Bergman, E. A., Cambaz, M. D., Gaudreau, É., Karasözen, E., &
689 Tan, F., 2020. The 2020 M_w 6.8 Elazığ (Turkey) Earthquake Reveals Rupture Behavior of the
690 East Anatolian Fault, *Geophys. Res. Lett.*, **47**(13), e88136.
- 691 Press, W. H., Flannery, B. P., Teukolsky, S. A., & Vetterling, W. T., 1992. Numeric recipes in C:
692 the art of scientific computing, *Camb. Univ. Press Camb*.
- 693 Ran, H., Shanguan, W., & Liu, D., 2020. Location study of Xinjiang Jiashi Ms6.4 earthquake
694 and aftershocks sequence on January 19th, 2020, *Inland Earthquake*, **34**(1), 56–61.
- 695 Ran, Y., Yang, X., Xu, X., Cheng, J., & Chen, L., 2006. Deformation pattern and shortening

- 696 rates in the east part of Kalpin Thrust system in southwest Tianshan during late Quaternary,
697 *Seismology and Geology (in Chinese with English abstract)*, **28(2)**, 179–193.
- 698 Reigber, C., Michel, G. W., Galas, R., Angermann, D., Klotz, J., Chen, J. Y., Papschev, A., Ar-
699 slanov, R., Tzurkov, V. E., & Ishanov, M. C., 2001. New space geodetic constraints on the
700 distribution of deformation in Central Asia, *Earth and Planetary Science Letters*, **191(1-2)**,
701 157–165.
- 702 Roustaei, M., Nissen, E., Abbassi, M., Gholamzadeh, A., Ghorashi, M., Tatar, M., Yamini-Fard,
703 F., Bergman, E., Jackson, J., & Parsons, B., 2010. The 2006 March 25 Fin earthquakes (Iran)-
704 insights into the vertical extents of faulting in the Zagros Simply Folded Belt, *Geophysical*
705 *Journal International*, **181(3)**, 1275–1291.
- 706 Semmane, F., Cotton, F., & Campillo, M., 2005. The 2000 Tottori earthquake: A shallow earth-
707 quake with no surface rupture and slip properties controlled by depth, *Journal of Geophysical*
708 *Research: Solid Earth*, **110(3)**, 1–13.
- 709 Sloan, R. A., Jackson, J. A., Mckenzie, D., & Priestley, K., 2011. Earthquake depth distribu-
710 tions in central Asia, and their relations with lithosphere thickness, shortening and extension,
711 *Geophysical Journal International*, **185(1)**, 1–29.
- 712 Tong, X., Sandwell, D. T., & Fialko, Y., 2010. Coseismic slip model of the 2008 Wenchuan
713 earthquake derived from joint inversion of interferometric synthetic aperture radar, GPS, and
714 field data, *Journal of Geophysical Research*, **115(B4)**, 1–19.
- 715 Walker, R., Jackson, J., & Baker, C., 2003. Surface expression of thrust faulting in eastern Iran:
716 source parameters and surface deformation of the 1978 Tabas and 1968 Ferdows earthquake
717 sequences, *Geophysical Journal International*, **152(3)**, 749–765.
- 718 Walker, R. T., Bergman, E. A., Szeliga, W., & Fielding, E. J., 2011. Insights into the 1968-
719 1997 Dasht-e-Bayaz and Zirkuh earthquake sequences, eastern Iran, from calibrated relocations,
720 InSAR and high-resolution satellite imagery, *Geophysical Journal International*, **187(3)**, 1577–
721 1603.
- 722 Wang, D., Zhao, B., Yu, J., & Tan, K., 2020. Active tectonic deformation around the Tarim Basin
723 inferred from dense GPS measurements, *Geodesy and Geodynamics*, **11(6)**, 418–425.

- 724 Wei, S., Barbot, S., Graves, R., Lienkaemper, J. J., Wang, T., Hudnut, K., Fu, Y., & Helmberger,
725 D., 2015. The 2014 Mw 6.1 South Napa Earthquake: A unilateral rupture with shallow asperity
726 and rapid afterslip, *Seismological Research Letters*, **86**(2A), 344–354.
- 727 Werner, C., Wegmüller, U., Strozzi, T., & Wiesmann, A., 2000. Gamma SAR and interferometric
728 processing software, in *Proceedings of the ERS-ENVISAT symposium, Gothenburg, Sweden*.
- 729 Wessel, P., Luis, J., Uieda, L., Scharroo, R., Wobbe, F., Smith, W., & Tian, D., 2019. The generic
730 mapping tools version 6, *Geochemistry, Geophysics, Geosystems*, **20**(11), 5556–5564.
- 731 Weston, J., Ferreira, A. M. G., & Funning, G. J., 2011. Global compilation of interferometric syn-
732 thetic aperture radar earthquake source models: 1. Comparisons with seismic catalogs, *Journal*
733 *of Geophysical Research: Solid Earth*, **116**(B8), B08408.
- 734 Wimpenny, S. & Scott Watson, C., 2020. gWFM: A global catalog of moderate-magnitude earth-
735 quakes studied using teleseismic body waves, *Seismological Research Letters*, **92**(1), 212–226.
- 736 Windley, B. F., Allen, M. B., Zhang, C., Zhao, Z. Y., & Wang, G. R., 1990. Paleozoic accretion
737 and Cenozoic reformation of the Chinese Tien Shan Range, central Asia.
- 738 Wright, T. J., Parsons, B. E., Jackson, J. A., Haynes, M., Fielding, E. J., England, P. C., & Clarke,
739 P. J., 1999. Source parameters of the 1 October 1995 Dinar (Turkey) earthquake from SAR
740 interferometry and seismic bodywave modelling, *Earth and Planetary Science Letters*, **172**(1-
741 2), 23–37.
- 742 Wright, T. J., Lu, Z., & Wicks, C., 2004. Constraining the slip distribution and fault geometry of
743 the Mw 7.9, 3 November 2002, Denali fault earthquake with Interferometric Synthetic Aperture
744 Radar and Global Positioning System data, *Bulletin of the Seismological Society of America*,
745 **94**(6 SUPPL. B), 175–189.
- 746 Xinjiang Bureau of Geology and Mineral Resources, 1993. *Regional Geology of Xinjiang Uygur*
747 *Autonomous Region*, Geological Publishing House, Beijing.
- 748 Xu, Y., Roecker, S. W., Wei, R., Zhang, W., & Wei, B., 2006. Analysis of seismic activity in the
749 crust from earthquake relocation in the central Tien Shan, *Bulletin of the Seismological Society*
750 *of America*, **96**(2), 737–744.
- 751 Yang, H., Li, Y., Shi, J., Xiao, A., Huang, S., Wu, G., Wang, H., Wang, X., Zhao, Y., & Liu,

- 752 Y., 2010. Tectonic characteristics of the Late Cenozoic south Tianshan fold-and-thrust belt,
753 *Quaternary Sciences*, **30**(5), 1030–1043 (in Chinese with English abstract).
- 754 Yang, X., Ran, Y., Song, F., Xu, X., Cheng, J., Min, W., Han, Z., & Chen, L., 2006. The analysis
755 for crust shortening of Kalpin Thrust tectonic zone, south-western Tianshan, Xinjiang, China,
756 *Seismology and Geology (in Chinese with English abstract)*, **28**(2), 194–204.
- 757 Yang, Z. X., Zhao, J. R., Zhang, X. K., Zhang, C. K., Cheng, S. X., Duan, Y. L., Zhang, J. S., &
758 Wang, S. J., 2002. Tomographic determination of the upper crustal structure in the Jiashi strong
759 earthquake swarm region, *Acta Seismologica Sinica English Edition*, **15**(2), 162–170.
- 760 Yao, Q., Yang, W., Jiang, X., Guo, Y., Liu, J., Zhang, Y., Wang, H., Ren, J., Yu, C., Yue, C.,
761 & Zhao, J., 2021a. The 2020 M6.4 Jiashi Earthquake: An Event that Occurred Under the
762 Décollement on the Kaping Fold-and-Thrust Belt in the Southwestern Tien Shan Mountains,
763 China, *Frontiers in Earth Science*, **9**(May), 1–14.
- 764 Yao, Y., Wen, S., Li, T., & Wang, C., 2021b. The 2020 Mw6.0 Jiashi earthquake: A fold earth-
765 quake event in the southern Tian Shan, northwest China, *Seismological Research Letters*, **92**(2),
766 859–869.
- 767 Yin, A., Craig, P., Harrison, T. M., Ryerson, F. J., Qian, X., & Yang, G., 1998. Late Cenozoic
768 tectonic evolution of the southern Chinese Tian Shan, *Tectonics*, **17**(1), 1–27.
- 769 Yu, P., Qiao, X., Xiong, W., Chen, W., Nie, Z., Wang, D., Jia, Z., & Li, J., 2020. Source model
770 for the M w 6.0 earthquake in Jiashi, China on 19 January 2020 from Sentinel-1A InSAR data,
771 *Earth, Planets and Space*, **72**(1).
- 772 Zhang, G., Zhu, L., Song, X., Li, Z., Yang, M., Su, N., & Chen, X., 1999. Predictions of the 1997
773 strong earthquakes in Jiashi, Xinjiang, China, *Bulletin of the Seismological Society of America*,
774 **89**(5), 1171–1183.
- 775 Zhang, Z. Q., Chen, J. Y. S., & Lin, J., 2008. Stress interactions between normal faults and
776 adjacent strike-slip faults of 1997 Jiashi earthquake swarm, *Science in China, Series D: Earth
777 Sciences*, **51**(3), 431–440.
- 778 Zhou, S. Y. & Xu, Z. H., 2000. Fracture characteristics of the 1997 Jiashi, Xinjiang, China, earth-
779 quake swarm inferred from source spectra, *Acta Seismologica Sinica English Edition*, **13**(2),

780 125–135.

781 Zhou, Z., Kusky, T. M., & Tang, C.-C., 2019. Coulomb stress change pattern and aftershock
782 distributions associated with a blind low-angle megathrust fault, Nepalese Himalaya, *Tectono-*
783 *physics*, **767**, 228161.

784 Zubovich, A. V., Wang, X. Q., Scherba, Y. G., Schelochkov, G. G., Reilinger, R., Reigber, C.,
785 Mosienko, O. I., Molnar, P., Michajljow, W., Makarov, V. I., Li, J., Kuzikov, S. I., Herring,
786 T. A., Hamburger, M. W., Hager, B. H., Dang, Y. M., Bragin, V. D., & Beisenbaev, R. T., 2010.
787 GPS velocity field for the Tien Shan and surrounding regions, *Tectonics*, **29**(6), 1–23.